

Variations in Volatile-Driven Activity of Comet C/2017 K2 (PanSTARRS) Revealed by Long-Term Multi-Wavelength Observations

S. Hmiddouch^{1,2*}, E. Jehin¹, M. Lippi³, M. Vander Donckt¹, K. Aravind¹, D. Hutsemékers¹, J. Manfroid¹, A. Jabiri², Y. Moulane⁴, and Z. Benkhaldoun²

¹ Space sciences, Technologies & Astrophysics Research (STAR) Institute, University of Liège, Liège, Belgium

² Cadi Ayyad University (UCA), Oukaimeden Observatory (OUCA), Faculté des Sciences Semlalia (FSSM), High Energy Physics, Astrophysics and Geoscience Laboratory (LPHEAG), Marrakech, Morocco

³ INAF – Osservatorio Astrofisico di Arcetri – Largo Enrico Fermi, 5, 50125 Firenze, Italy

⁴ School of Applied and Engineering Physics, Mohammed VI Polytechnic University, Ben Guerir 43150, Morocco

*e-mail: shmiddouch@uliege.be

Received/accepted

ABSTRACT

Context. By conducting a comprehensive study of comets across a broad range of heliocentric distances, we can improve our understanding of the physical mechanisms that trigger their activity at various distances from the Sun. At the same time, we can identify possible differences in the composition of these outer solar system bodies belonging to various dynamical groups. C/2017 K2 (PANSTARRS) is a Dynamically New Oort Cloud comet (DNC) that has exhibited activity at an extremely large heliocentric distance of 23.75 au, was found to have a CO-rich coma at 6.72 au, and attracted the interest of the community to become a bright DNC at perihelion.

Aims. We aim to study through photometry and spectroscopy the activity evolution and chemical composition of C/2017 K2 over a long-term monitoring from October 2017 ($r_h = 15.18$ au) pre-perihelion to April 2025 ($r_h = 8.46$ au) post-perihelion.

Methods. We used both TRAPPIST telescopes to monitor the activity with broad-band and cometary narrow-band filters. We produced an 8-year light curve and colors from the broad-band images and computed the activity slopes. We derived the production rates of the daughter species, OH, NH, CN, C₃, and C₂, using a Haser model as well as the dust proxy parameter $A(0)f_0$. We used CRILES⁺, the high-resolution infrared echelle spectrometer of the ESO VLT, and UVES, its high-resolution ultraviolet-visual echelle spectrograph, to study simultaneously the parent and daughter species, at three different epochs from May to September 2022, when the comet crossed the water sublimation region.

Results. C/2017 K2 (PanSTARRS) light curve shows a complex evolution of its brightness, with several slopes and a plateau around perihelion, revealing the onset and competition of various species. The photometric analysis shows constant coma colors across the whole heliocentric range, indicating similar properties of the dust grains released during the survey, and in agreement with the colors of other active long-period comets. The production rates indicate a typical C₂/CN composition and a high dust-to-gas ratio. The analysis of the oxygen forbidden lines shows the transition between CO and CO₂ dominating the comet's activity to the onset of the water sublimation below 3.0 au. Molecular abundance analysis from the IR spectra classified C/2017 K2 as a typical-to-enriched comet, with HCN identified as the main parent molecule of CN, and C₂ probably originating from C₂H₂ rather than C₂H₆.

Key words. Comets: general - Comets: individual: C/2017 K2 (PanSTARRS) - Techniques: photometric - Techniques: spectroscopic

1. Introduction

Comets are preserved relics from the primordial phases of the solar system's formation, having condensed from icy and dusty material surrounding the proto-Sun approximately 4.6 billion years ago. Consequently, they provide direct evidence of material from this era. Following their formation, significant gravitational interactions with the giant planets caused their dispersion into present reservoirs, namely the Kuiper Belt (the source of the ecliptic Jupiter Family Comets) and the Oort Cloud (the source of isotropic Long period comets). These frozen nuclei are believed to have retained the majority of their chemical and mineralogical properties associated with their region of origin within the protoplanetary disk, thereby offering invaluable insights into the initial phases of the solar system (Gomes et al. 2005; Morbidelli et al. 2007).

The most abundant volatile in comets, water, can only sublimate at temperatures present within 3.0 au of the Sun, as originally suggested in the "dirty snowball" model of the nucleus (Whipple 1950). For comets active at greater distances, more volatile species such as CO or CO₂ must be sublimating, or another mechanism such as ice crystallization or non-thermal processes must be at play (Jewitt et al. 2019).

An example of such a distant active comet is C/2017 K2 (PanSTARRS), hereafter K2, an Oort cloud comet, discovered by the Pan-STARRS survey (Kaiser & Pan-STARRS Team 2002) in May 2017, when it was at a heliocentric distance of $r_h=16.1$ au (Wainscoat et al. 2017). Prediscovery images of K2 were found showing the comet exhibiting activity at an extremely large distance of 23.8 au in May 2013 (Jewitt et al. 2017; Meech et al. 2017; Hui et al. 2018). Comet K2 is the second-most distant discovery of an active comet. At such a distance,

Table 1: TRAPPIST observational circumstances and orbital elements of comet C/2017 K2.

Comet	i (°)	T _J	Peri (au)	T _p (UTC)	r _h -range Pre/Post (au)	Dates Start/End	Number of nights TN	Number of images TS	Number of nights TN	Number of images TS
C/2017 K2 (PanSTARRS)	87.55	0.17	1.79	19.12.2022	15.18 - 1.79 - 8.46	25.10.2017 - 20.04.2025	151	120	1323	881

Note: i: Inclination, T_J: Jupiter-Tisserand invariant, Peri: Perihelion distance, T_p: Time of perihelion passage. The format of the date is Day.Month.Year

the activity cannot be driven by the sublimation of water ice in the nucleus, which is the principal mechanism for comets in the inner solar system. The sublimation of super-volatile ice, including CO, CO₂, N₂ and O₂, drives the ejection of dust and gas, resulting in detectable cometary activity even at extreme distances from the Sun (Jewitt et al. 2017). Sub-millimeter observations later confirmed the presence of carbon monoxide (CO) in K2's coma with $Q_{CO} = (1.6 \pm 0.5) \times 10^{27}$ at $r_h = 6.72$ au (Yang et al. 2021).

Królikowska & Dybczyński (2018), performed dynamical simulations showing that K2 has probably never previously entered the inner solar system ($r_h \leq 5$ au) where substantial sublimation on the nucleus can take place. Its original semi-major axis is now estimated to be as large as 28000 au (Combi et al. 2025), which, following the definition of A'Hearn et al. (1995) (>20000 au), should then be classified as a Dynamically New Comet (DNC). Photometric analyses have suggested that DNCs tend to behave differently from returning comets and often exhibit more asymmetric light curves that are substantially brighter before than after perihelion (Holt et al. (2024), Hmiedouch et al. (2024)). Such differences in photometric behavior may arise from intrinsic variations in the nucleus and coma properties affected by thermal processing in the inner solar system. K2's brightness while still in the outer Solar System makes it a particularly compelling target for evaluating the effects of solar heating on the properties of a relatively fresh comet (Zhang et al. 2022). It is also important to study the activity behavior of DNCs and composition from far away down to perihelion in the context of the new ESA F-class mission, Comet Interceptor (Jones et al. 2024). This mission will flyby a pristine comet visiting for the first time the inner solar system, to better understand those comets and their peculiarities.

2. Observation and data reduction

2.1. Photometry (TRAPPIST)

We used both TRAPPIST¹ (TRAnsiting Planets and Planetesimals Small Telescopes) North and South, hereafter TN and TS (Jehin et al. 2011), to observe and follow comet K2 for almost eight years. TRAPPIST-South is equipped with a 2K×2K FLI Proline CCD with a pixel scale of 0.65 arcsec/pixel, resulting in a FOV of 22'×22', while TRAPPIST-North is equipped with an Andor IKONL BEX2 DD (0.59 arcsec/pixel) with a 20'×20' field of view.

The observations were carried out with a binning of 2X2, resulting in a plate scale of 1.30 and 1.20 arcsec/pixel, respectively. In addition to the standard Johnson-Cousin B, V, Rc, and Ic broad-band filters, the telescopes are also equipped with cometary HB narrow-band filters that were specifically designed for observing comet Hale-Bopp (Farnham et al. 2000). These

narrowband filters isolate emissions from OH (309.7 nm), NH (336.1 nm), CN (386.9 nm), C₃ (406.3 nm) and C₂ (513.5 nm), as well as three emission-free wavelength regions (BC at 445.3 nm, GC at 525.9 nm and RC at 713.3 nm).

Our observations of comet K2 began with the TN telescope on October 25, 2017, using broad-band filters. At that time, the comet was at a distance of 15.18 au from the Sun and had a visual magnitude of 19.7. We continued observing the comet with both broadband and HB narrowband filters using the TS telescope starting on September 9, 2021, when it became visible and bright enough from the southern hemisphere ($r_h = 5.4$ au). We monitored the comet about two times a week until October 24, 2022, when it became too low in the sky and was not visible due to its solar conjunction. After perihelion on December 19, 2022 ($r_h = 1.79$ au), we recovered the comet on January 27, 2023. We continued observing it as long as it remained bright and high enough in the sky, until May 3, 2023 ($r_h = 2.46$ au). Then we continued to monitor its activity until April 2025 ($r_h = 8.46$ au) with only the broad-band filters.

Overall, we collected about 2204 broad-band images and 174 narrow-band images of the comet over a total of 271 nights, spending 8 years (Table 1). The exposure times ranged from 30 to 240 seconds for the broad-band filters and from 300 to 1500 seconds for the narrow-band filters based on the brightness of the comet as it approached or moved away from the Sun. The data were calibrated using standard procedures, such as subtracting bias, dark, and performing flat-field correction. The sky contamination was then removed, and the data were flux calibrated using standard stars observed regularly during the same period, using the same procedure explained in previous TRAPPIST publications (Opitom et al. 2015; Moulane et al. 2018). After the determination of the comet's photocenter, we derived median radial brightness profiles from the gas and dust images. Then, we removed dust contamination from the gas radial profiles using images of comets in the BC filter, because it is less contaminated by cometary gas emission than the other dust filters (Farnham et al. 2000). The fluxes of OH, NH, CN, C₃, and C₂ were converted into column densities, and we fitted a Haser model (Haser 1957) to the profiles to derive the production rates. The Haser model, although not physically accurate as it assumes the one-step photo-dissociation of the parent molecule into daughter molecules in a spherically symmetric coma, is commonly used to determine the gas production rates from optical comet observations. It enables comparisons between observations made by various observers, as well as comparisons between different comets. The model adjustment is performed at a nucleocentric distance of around 10,000 km to avoid PSF and seeing effects around the photocenter. At greater nucleocentric distances, the signal usually becomes fainter, especially in the OH filter, for which the signal-to-noise ratio (S/N) is lower. Fluorescence efficiencies (also called g-factors) from David Schleicher's web-

¹ <https://www.trappist.uliege.be/>

site² (see also Table B.1) were used to convert fluxes into column densities. The C_2 g-factor is determined only by considering C_2 in a triplet state, as noted by A'Hearn (1982). Similarly, the C_3 g-factor were also determined by A'Hearn (1982). CN and NH fluorescence efficiencies vary with both the heliocentric distance and the velocity and are taken, respectively, from Schleicher (2010) and Meier et al. (1998). The value of the g-factor for the OH (0-0) band centered near 3090 Å varies with both the heliocentric distance and velocity (Schleicher & A'Hearn 1988). We used scale lengths from A'Hearn et al. (1995) scaled as r_h^2 . The choice of using scale lengths, with r as heliocentric distance, was made to facilitate comparison with various data sets, particularly the extensive data set from A'Hearn et al. (1995).

We used broad-band filters including B, V, Rc, and Ic (Bessell 1990) to monitor the evolution of the light curve in various colors over almost eight years. We used observations with the narrow-band BC, GC, and RC filters and also with the broad-band Rc filter to estimate dust production. From the dust profiles, we derived the $Af\rho$ parameter, as first introduced by A'Hearn et al. (1984). All $Af\rho$ values were corrected for the phase angle to obtain $A(0)f\rho$. Several phase functions have been proposed (Divine 1981; Hanner & Newburn 1989; Schleicher et al. 1998 or Marcus 2007). We used the phase function described by Schleicher³, which is a combination of two different phase functions of Schleicher et al. 1998 and Marcus 2007.

2.2. Optical spectroscopy with UVES at UT2/VLT

To conduct a detailed investigation of the composition of K2 in the optical range and its evolution while getting closer to perihelion, we conducted a program with the high-resolution Ultraviolet-Visual Echelle Spectrograph (UVES) on the Unit 2 telescope (UT2) of the ESO 8-m VLT, at Paranal on three different epochs before and after the water sublimation line (~ 3 au). We used two distinct UVES standard settings to achieve a complete optical range coverage (303-1060 nm): the dichroic #1 (346 + 580), which goes from 303 to 388 nm in the blue and 476 nm to 684 nm in the red, and the dichroic #2 setting (437 + 860), covering 373 to 499 nm in the blue and 660 to 1060 nm in the red. The details of these spectral observations are summarized in Table 3. We used a $0.45'' \times 10''$ slit in the blue, resulting in a resolution power of $\sim 70,000$, and a $0.45'' \times 12''$ slit in the red, resulting in a resolution power of $\sim 90,000$. The slit was centered on the inner coma and aligned with the Sun direction.

We processed the data using the ESO UVES pipeline (Ballester et al. 2000), supplemented with custom routines for extraction and cosmic ray removal, followed by correction for the Doppler shift due to the comet's relative velocity to Earth. The spectra were calibrated in absolute flux using either the archived master response curve or a response curve derived from a standard star observed near the science spectrum. Finally, the continuum, including sunlight reflected by cometary dust grains, was removed using the BASS2000⁴ solar spectrum, adjusted to match the comet slope. Consequently, the final spectrum includes only the gas component. More details on the data reduction process are available in Manfroid et al. (2021) and references therein.

2.3. NIR spectroscopy with CRIRES+ at UT3/VLT

CRIRES+, mounted on the Unit 3 telescope (UT3) at the VLT, is the ESO high-resolution infrared 0.95–5.3 μm spectrograph. This upgraded version of the original CRIRES instrument (Kaeufl et al. 2004; Dorn et al. 2014), is now a cross-dispersed echelle spectrometer, offering ten times greater wavelength coverage than its previous version while maintaining a high spectral resolving power of 40,000 for a slit width of $0.4''$. The enhanced CRIRES+ is equipped with three new detectors, providing a larger field coverage area, lower noise, higher quantum efficiency, and reduced dark current. Performance is further enhanced by the multi-application curvature adaptive optic system (MACAO) (Paufigue et al. 2004).

Table 2: The simultaneous UVES and CRIRES+ observational circumstances of comet C/2017 K2, with the UT2 and UT3 telescopes of the ESO VLT.

Date 2022	r_h (au)	r_Δ (au)	r_Δ (km/s)
May 9	3.23	2.66	-37.7
July 5	2.73	1.82	-6.65
Sept 21	2.12	2.32	15.98
Sept 22	2.11	2.35	15.6

Observations of K2 were conducted using CRIRES+ over three nights, simultaneously with UVES observations, as detailed in Tables 2, and 3. The settings were selected to capture the majority of primary volatiles (e.g., H_2O , CO, C_2H_6 , CH_4 , HCN, NH_3 , etc.) and to monitor their evolution as the comet approaches the Sun (Lippi et al. 2023). We used a slit of $0.4''$, aligned along the extended Sun-comet radius vector.

Data were processed using custom semi-automated procedures (see Villanueva et al. 2011, 2022; Bonev 2005), enabling efficient spectral analysis. Spectral calibration and correction for telluric absorption were performed by comparing the data to highly accurate atmospheric radiance and transmittance models generated with PUMAS/PSG (Villanueva et al. 2018). Flux calibration was achieved using the spectra of a standard star observed close in time to the comet and processed with the same algorithms. Production rates and relative abundances (i.e., mixing ratios relative to water) of various primary species in the coma were determined as described in Lippi et al. (2020) (and references therein), using advanced fluorescence models (e.g., Villanueva et al. (2012), Radeva et al. (2011)). Figure C.1 shows a selection of K2 spectra acquired with CRIRES+.

3. Data analysis and results

3.1. Photometry (TRAPPIST)

In this section, we present the comet K2 light curves in different filters as well as the evolution of its activity and composition before and after perihelion.

3.1.1. Light curves and coma dust colors

Figure B.1, presents the evolution of the magnitude in a 5 arcsec aperture, using the B, V, Rc, and Ic broadband filters compared to the magnitude reported in the JPL ephemeris. The data are fitted using the standard magnitude formula " $M = M_0 + 5 \times \log_{10}(r_\Delta) +$

² <https://asteroid.lowell.edu/comet/gfactor.html>

³ <https://asteroid.lowell.edu/comet/dustphase.html>

⁴ https://bass2000.obspm.fr/solar_spect.php

Table 3: CRIRES⁺ and UVES observation log

Date	Instrument	Setting	Airmass	Exposure time [s]
9 May. 2022	CRIRES ⁺	L3377	1.130	2280
	CRIRES ⁺	M4318	1.115	1400
	UVES	346+580	1.24	3000
	UVES	437+860	1.28	3000
5 July 2022	CRIRES ⁺	L3377	1.130	3600
	CRIRES ⁺	M4318	1.115	2880
	UVES (a)	437+860	1.28	3000
	UVES (a)	346+580	1.15	3000
	UVES (b)	346+580	1.11	3600
21 Sep. 2022	UVES (b)	437+860	1.13	3600
	CRIRES ⁺	L3377	1.375	2400
	CRIRES ⁺	M4318	1.720	1600
	UVES	346+580	1.34	3000
22 Sep. 2022	UVES	437+860	1.71	3000
	CRIRES ⁺	L3377	1.595	2640
	CRIRES ⁺	L3302	1.288	2880
	UVES	346+580	1.29	3600
	UVES	437+860	1.66	3600

Note:(a) and (b) are two different UVES observations executed during the same night.

$2.5 \times n \times \log_{10}(r_h)$ ", using the best fit parameters; n is a coefficient and M_0 the absolute magnitude. r_Δ and r_h are the geocentric and heliocentric distances, respectively. K2 was observed in the four-band filters for its entire inner solar system passage. The comet reached its peak brightness, corresponding to an Rc-band magnitude of 11.18 on January 30, 2023. The light curve shows large-scale deviations but no outbursts. It was not possible to observe the comet the month before and after perihelion due to its conjunction with the Sun.

Figure 1 shows the color indices B-V, B-R, V-R, and R-I, or colors in short, of K2 as a function of the heliocentric distance. The colors are surprisingly constant throughout the whole range of heliocentric distances, except near the perihelion (< 2.0 au) where the B and V filters are contaminated by the gaseous emission of CN and C₂ respectively. This means that the properties of the dust (such as grain size) do not change much in the small aperture centered on the nucleus. The colors agree very well with those measured for 25 long-period active comets (LPC) by Jewitt (2015) (see Table 4, and Figure 2). We divided the comets in Jewitt (2015) into two groups: 13 dynamically new comets (DNCs) and 12 returning comets (RCs), and compared their broadband colors with those of comet K2 (see Figure 2). Our analysis reveals no significant color differences between the two dynamical classes, which is also consistent with the result from Holt et al. (2024) for 21 LPCs. The colors do not allow for distinguishing comets from different dynamical origins. We may note that K2 lies on the blue side of the distribution of colors.

To investigate the temporal evolution of the comet's photometric activity, we performed linear fits over four distinct time intervals relative to perihelion (see Figure 3, and Table 5). Each interval corresponds to a different phase in the comet's activity: Distant pre-perihelion phase from -1880 to -500 days (from 15.18 to 5.3 au): The comet shows a slow and steady brightening trend. This behavior likely corresponds to the early onset of activity, dominated by the sublimation of highly volatile ices (e.g., CO, CO₂) at large heliocentric distances. The activity is weak, but measurable, with a low negative slope indicating increasing brightness.

Approaching perihelion from -360 to -160 days (from 4.29 to 2.71 au): A sudden and more pronounced brightening is observed, reflected by a steeper negative slope. This phase is characterized by a rapid increase in activity, likely driven by the onset of water-ice sublimation and increased dust production. The

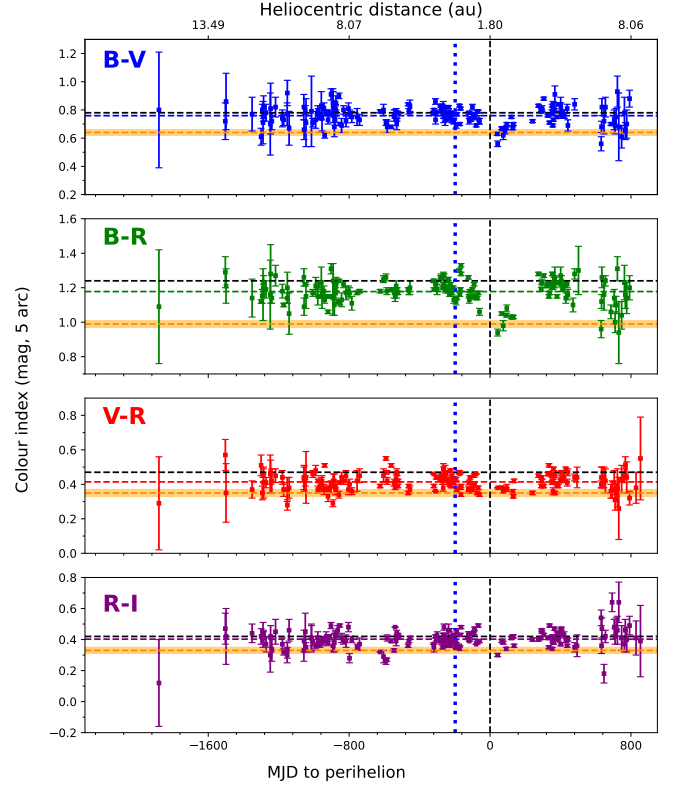


Fig. 1: B-V, B-R, V-R, and R-I colors of C/2017 K2 vs time to perihelion and heliocentric distance, with the mean values from Table 4 compared with the average value of 25 active LPC from Jewitt (2015) (black horizontal dashed lines), and the Sun colors from Holmberg et al. (2006) (orange horizontal dashed lines). The vertical dashed line represents the perihelion, and the vertical blue dotted line represents the water ice sublimation boundary (~ 3 au).

Table 4: Comparison of C/2017 K2 colors with active LPCs

Object	B - V	V - R	R - I	B - R
C/2017 K2	0.76 ± 0.06	0.42 ± 0.04	0.40 ± 0.05	1.18 ± 0.06
DNCs	0.76 ± 0.05	0.49 ± 0.05	0.42 ± 0.02	1.26 ± 0.07
RCs	0.80 ± 0.05	0.48 ± 0.05	0.37 ± 0.09	1.28 ± 0.05
Active LPCs	0.78 ± 0.02	0.47 ± 0.02	0.42 ± 0.03	1.24 ± 0.02
Sun	0.64 ± 0.02	0.35 ± 0.01	0.33 ± 0.01	0.99 ± 0.02

Note: The mean colors of C/2017 K2 are compared to the mean colors of DNC and returning comets from the sample of 25 LPC from Jewitt (2015). The Sun color is from Holmberg et al. (2006).

higher correlation (R^2) suggests that the linear model fits this interval well, indicating a relatively smooth ramp-up in activity. Near-perihelion plateau from -130 to -50 days (from 2.37 to 1.96 au): The fit yields a nearly flat slope, indicating a stable and plateau phase in the brightness and activity of the comet. This disappointing performance of the comet, which was expected to be brighter at perihelion, was noticed by many. This may sug-

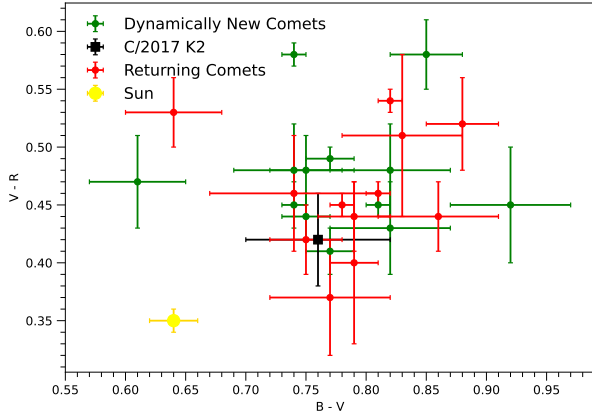


Fig. 2: Color-color plot comparing C/2017 K2 (square) with dynamically new comets (green) and returning comets (red) from Jewitt (2015). The color of the Sun is marked by a yellow circle.

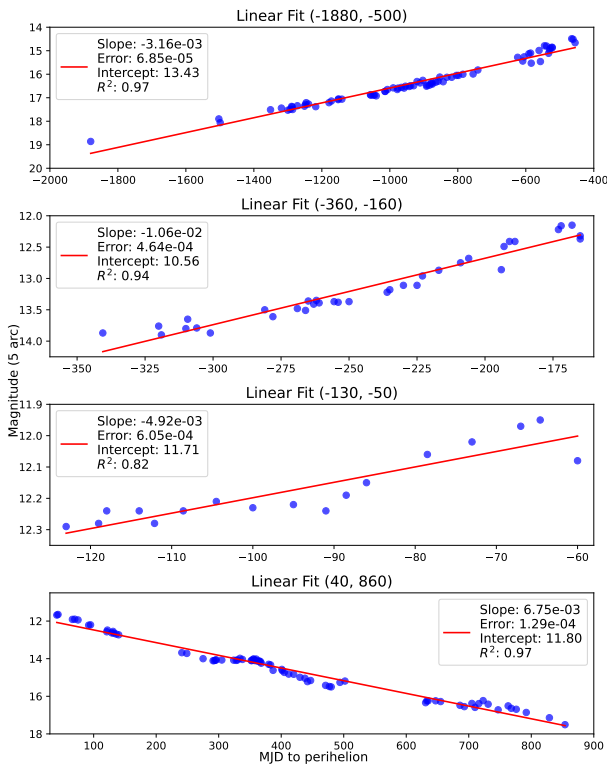


Fig. 3: The four different slope regimes in the Rc light curve of comet C/2017 K2.

Table 5: Slope fitting results in the light curve evolution of comet C/2017 K2.

Days to perihelion	r_h -range (au)	Best Slope	Intercept	R-squared
-1880, -500	15.18 - 5.3	$-3.16 \pm 0.068 \times 10^{-3}$	13.43	0.97
-360, -160	4.29 - 2.71	$-1.06 \pm 0.046 \times 10^{-2}$	10.56	0.94
-130, -50	2.37 - 1.96	$-4.92 \pm 0.60 \times 10^{-3}$	11.71	0.82
40, 860	1.87 - 8.46	$6.75 \pm 0.13 \times 10^{-3}$	11.80	0.97

gest a temporary equilibrium between solar input and gas/dust production. The low correlation indicates the presence of more complex or possibly non-linear behavior during this transitional

phase.

Post-perihelion decline from +40 to +460 days (from 1.87 to 8.46 au): After perihelion, the comet shows a larger slope and a fast fading. This decline is expected as the heliocentric distance increases and solar heating diminishes. The linear fit captures this trend well, with a consistent decrease in brightness over time. We note only one slope after perihelion.

3.1.2. Gas production rates, $A_f \rho$ and their ratios

Figure 4 illustrates the production rates of several volatile species (OH, NH, C_3 , CN, and C_2) in comet K2. The x-axis denotes the time to perihelion and the heliocentric distance, with a vertical dashed line indicating the perihelion at 1.79 au. The y-axis displays the logarithmic production rates in molecules per second, representing the outgassing rates for each species. For visibility, the OH production is scaled down by a factor of 10. The logarithmic scale facilitates the comparison of species with different production levels and highlights the comet's changing activity as it approaches or moves away from the Sun. The production rate values for the various species are summarized in Table A.1. We first detected CN and C_2 radicals at the end of March 2022 at 3.62 au, followed by the majority of other radicals that appeared in the coma about a month later, except for NH, which was observed only in mid-August 2022. The production rates gradually increased as the comet approached the Sun, from 3.62 to 2.71 au, and then it surprisingly stabilized, showing a plateau-like behavior both before and after perihelion, similar to the optical light curve.

Table 6: Average logarithmic production rates and $A(0)f\rho$ ratios of Comet C/2017 K2 in comparison with A'Hearn et al. (1995) Taxonomic Classes.

	C/2017 K2 (This work)	Typical comets (A'Hearn et al. 1995)	Depleted comets
C_2/CN	-0.037 ± 0.005	0.06 ± 0.10	-0.61 ± 0.35
C_2/OH	-2.65 ± 0.07	-2.44 ± 0.20	-3.30 ± 0.35
CN/OH	-2.58 ± 0.34	-2.50 ± 0.18	-2.69 ± 0.14
C_3/OH	-3.29 ± 0.07	-3.59 ± 0.29	-4.18 ± 0.28
NH/OH	-2.83 ± 0.14	-2.37 ± 0.27	-2.48 ± 0.34
$A(0)f\rho/OH$	-24.75 ± 0.43	-25.82 ± 0.40	-25.30 ± 0.29

Note: The $A(0)f\rho$ values used were computed from the images taken with the RC narrow-band filter.

CN remained detectable in our data until mid-October 2023 at 3.88 au, while C_2 and C_3 were no longer observed after early October at 3.83 au. OH was detected until September 20 at 3.69 au, while NH was detected until the end of March 2023 at 2.20 au. The OH, CN, and C_2 values are in good agreement with Combi et al. (2025) for the water production rates from SOHO measurements of the Lyman-alpha H line before and after perihelion, and with Schleicher's narrow band photometric measurements (private communication, see also Figure 4).

We calculated production rate ratios relative to CN and OH, as well as the dust-to-gas ratio. Comet K2 has a log $[A(0)f\rho/Q(OH)] = -24.75 \pm 0.43$, which places K2 in the dust-rich regime, compared to typical cometary values (Table 6) reported by A'Hearn et al. (1995). Figure 5 illustrates the evolution of the logarithm of C_2/CN over time to the perihelion

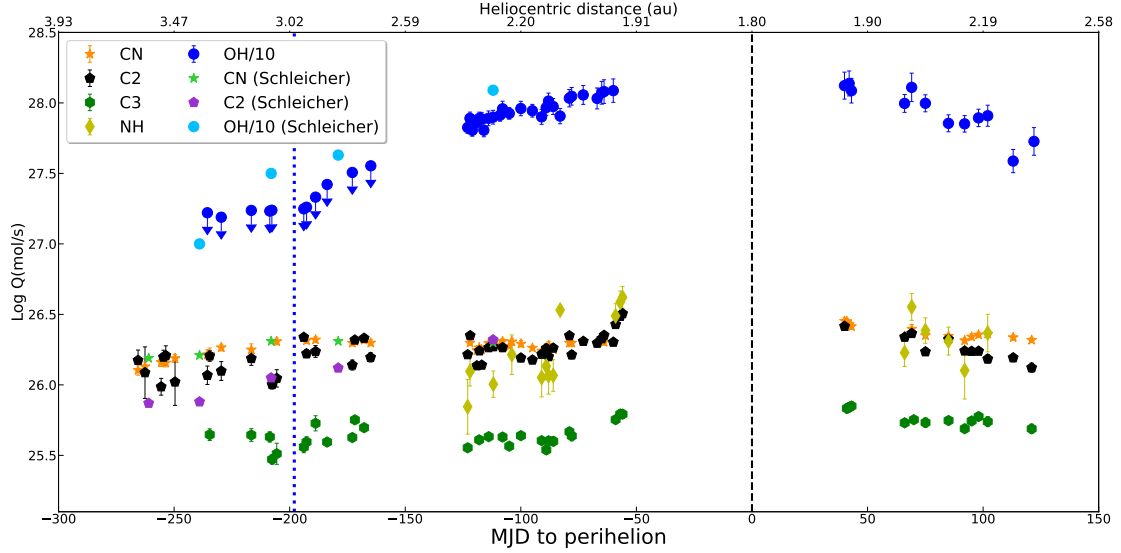


Fig. 4: OH, NH, CN, C₂, and C₃ logarithmic production rates of comet C/2017 K2 from TRAPPIST photometry as a function of time and the heliocentric distance. The vertical dashed line indicates the perihelion at 1.79 au on December 19, 2022.

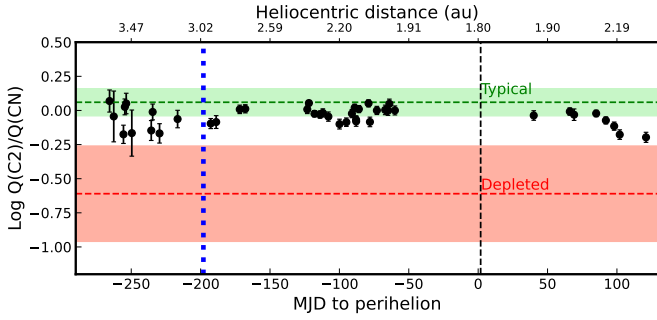


Fig. 5: The logarithm of C₂/CN production rate ratios of comet C/2017 K2, as a function of time and the heliocentric distance.

and heliocentric distances. According to the taxonomic classification by A’Hearn et al. (1995), the comet falls into the ‘typical’ group, which is defined by a characteristic abundance of C₂ and C₃ relative to CN and OH. Table 6 summarizes the production rates ratios in K2, compared to the comet database given in A’Hearn et al. (1995).

The apparent magnitude of a comet depends on its heliocentric distance, geocentric distance, and phase angle at the time of observation. To remove the influence of geometry and illumination effects, we computed the absolute magnitude (H), defined as the magnitude that the comet would have if observed at a heliocentric and geocentric distance of 1 au and a phase angle of 0°. It is given by:

$$H = m - 5 \log_{10}(r_h \times r_\Delta) - f(\alpha), \quad (1)$$

where m is the apparent magnitude in a given filter, r_h is the heliocentric distance, r_Δ is the geocentric distance. The phase correction $f(\alpha)$ is defined as $-2.5 \log_{10}[\phi(\alpha)]$, where $\phi(\alpha)$ is the phase function corresponding to the phase angle at the time of observation, as defined in Schleicher et al. (1998). Figure B.2 illustrates the variation in absolute magnitude of comet K2 as a function of days and distance to the perihelion.

The absolute magnitude in the Rc band can be used to derive the effective scattering cross-section (C_e) (Jewitt et al. 2019),

which provides insights into the dust content and activity of the comet. It is calculated as:

$$C_e = \frac{\pi r_0^2}{p} \cdot 10^{0.4[m_{\odot,R} - H_R]}, \quad (2)$$

where r_0 is the mean Earth–Sun distance in km, p is the geometric albedo of the dust, and $m_{\odot,R}$ is the apparent magnitude of the Sun in the Rc band. Using $r_0 = 1.5 \times 10^8$ km and $m_{\odot,R} = -26.97$ (Willmer 2018), this simplifies equation 2 to $C_e = (1.5 \times 10^6 / p) \times 10^{-(0.4H_R)}$. For this work, we adopt an albedo value of $p = 0.04$ based on estimates from Jewitt et al. (2019) and Zhang et al. (2019).

The effective scattering cross-section is further used to estimate the average dust mass loss rate via:

$$\frac{dM}{dt} = \frac{4}{3} \cdot \frac{\rho \bar{a} C_e}{\tau_r}, \quad (3)$$

where ρ is the bulk density of the dust particles, \bar{a} is the mean particle radius, and $\tau_r = L/v_{ej}$ is the residence time of the particles within an aperture of radius L , with v_{ej} being the ejection velocity. We adopt $\rho = 500$ kg/m³ and $\bar{a} = 100$ μ m, following Jewitt et al. (2019). A projected aperture radius of 5'' was used for the analysis, corresponding to a physical diameter that varies with the comet’s geocentric distance. Although dust velocity varies with heliocentric distance, for comparative purposes, we use a fixed ejection velocity of 14 m/s consistent with the average velocity for 100 μ m grains reported by Liu & Liu (2024).

On carefully analysing the variation of absolute magnitude as shown in Figure B.2, K2 displayed an unusual activity pattern as it approached the inner solar system. Initially, the comet appeared exceptionally bright at large distances (~ 15 au), exhibiting a low absolute magnitude, which suggests strong activity even in the outer solar system. This brightness was primarily driven by CO sublimation (Meech et al. 2017), which is consistent with the behaviour of the comet between 15 and 13 au, where the absolute magnitude decreased (the comet brightened). The same trend has also been reported by Jewitt et al. (2019) for observations at a similar heliocentric range. However, below 12 au, the absolute magnitude began to increase (the comet

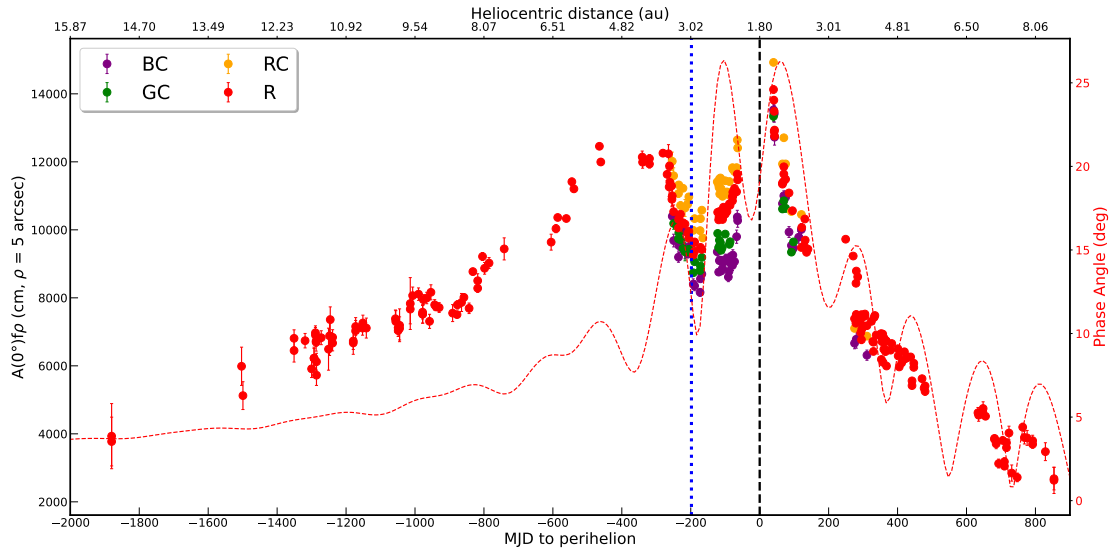


Fig. 6: The $A(0)f\rho$ parameter of comet C/2017 K2 from the broad- and narrow-band filters as a function of the heliocentric distance.

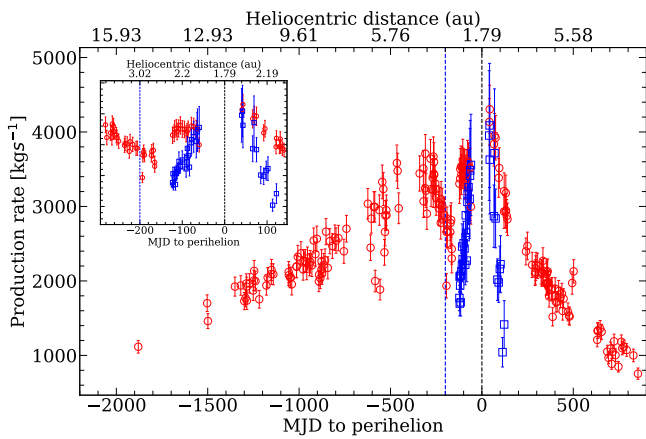


Fig. 7: The comparison of dust mass loss and water mass production in comet K2 as a function of days to perihelion. The dust mass loss was computed using equation 3, and water mass production was computed from the OH production rate observed by TRAPPIST. The vertical blue dotted line represents the water ice sublimation boundary (~ 3 au) (Womack et al. 2017; Crovisier & Encrenaz 2000), within which the main driving source of comet outgassing changes from supervolatile ices to H_2O ice (Kwon et al. 2023). The vertical dashed line represents the perihelion.

became fainter), indicating a decline in CO-driven activity. The most striking feature is the sharp increase in magnitude (fading) between 4 au and 3 au (see inset in Figure B.2). This can be attributed to the depletion of near-surface CO and/or CO_2 , which was the main driver of activity until then. Moreover, the non-detection of OH emission in the TRAPPIST and UVES observations before the comet crossed 3 au implies that water (H_2O) sublimation had not yet begun, creating a temporary lull in activity. Furthermore, in May ($r_h=3.23$ au), we did not see strong CO and H_2O lines in CRIRES⁺ spectra, which is in line with this hypothesis.

Once the comet approached closer to 3 au, the sublimation zone of water ice, the magnitude started to decrease again (brightening), signalling the onset of H_2O -driven activity. How-

ever, the comet did not become as bright as expected, as water production alone could not compensate for the loss of CO- and CO_2 - driven activity. The activity trend in $A(0)f\rho$ and gas production provides further evidence for this interpretation. Figure 6 shows the evolution of the dust proxy parameter $Af\rho$ in cm (A’Hearn et al. 1984) (see Table A.1), measured using the broad-band dust continuum filter (Rc), and the narrow-band dust continuum filters (RC, GC, BC). The vertical dashed line marks the comet perihelion at 1.79 au, where $A(0)f\rho$ reached a maximum of about 15000 cm, placing K2 among the very active LPC. Before perihelion, $A(0)f\rho$ shows a clear increase that is generally normal as the comet approaches the Sun, reflecting the increased dust release as a result of increased sublimation of ices.

However, a peculiar behavior is observed between -260 and -170 days to perihelion (3.60 to 2.74 au), where $Af\rho$ shows a strange drop followed by a rapid increase, suggesting some correlation with the phase angle. This apparently unusual trend persists even after accounting for the phase angle, suggesting that the phenomenon is intrinsic to the comet. Furthermore, the water production rate increased sharply around 3 au (see Figure 7) during which $Af\rho$ and the dust production also started to increase. In particular, it may indicate an exhaustion of CO and/or CO_2 ice at least in the near-surface layer, which typically drives sublimation activity between 3 and 6 au.

In any case, it is clear that the comet activity at the time of crossing the snowline underwent a loss of activity, as can be seen with the flattening of the light curve and the stall in the gas production rates. Kwon et al. (2024) observed the same trend using data from the ZTF IRSA archive⁵ (Masci et al. 2019), covering a range from ~ 14 to ~ 2.3 au. Although the trend is consistent, the $Af\rho$ values differ due to variations in photometry, likely caused by incorrect zero-point magnitude information used in their analysis (Kwon et al. (2024), personal communication). Post-perihelion, the $Af\rho$ displays a steep decrease with no correlation with the phase angle. This behaviour is usually observed for LPCs.

⁵ https://irsa.ipac.caltech.edu/applications/ztf/?_action=layout.showDropDown&

3.2. High Resolution Spectroscopy (VLT)

3.2.1. Optical spectroscopy with UVES

At the first epoch (May 9, 2022, $r_h=3.23$ au), only CN, C_3 , and C_2 are clearly detected with UVES, as in TRAPPIST images. Then at the second epoch (July 5, $r_h=2.73$ au), OH and all the usual other species start to be detected (NH, CH, NH_2). The emissions became much brighter at the last epoch (Sept 20, $r_h=2.12$ au) (see Figure 8). CO_2^+ ions are detected, but CO^+ ions are never detected, showing that K2 is not a CO^+ rich comet like C/2016 R2 observed at the same distance and whose optical spectrum was dominated by CO^+ bands (Opitom et al. 2019). But there could also be an observation bias, as we rarely observe CO^+ lines in the high-resolution spectra of UVES taken in the last two decades, because the slit is usually placed in the bright inner coma where the bands of the neutral species dominate and can hide the faint CO^+ lines. The slit is also tiny (10" in length), and geometrically it might be easy to miss the CO^+ thin asymmetric streams (only opposite to the Sun). When the slit is offset from the nucleus in the tail direction, ions can be observed more often.

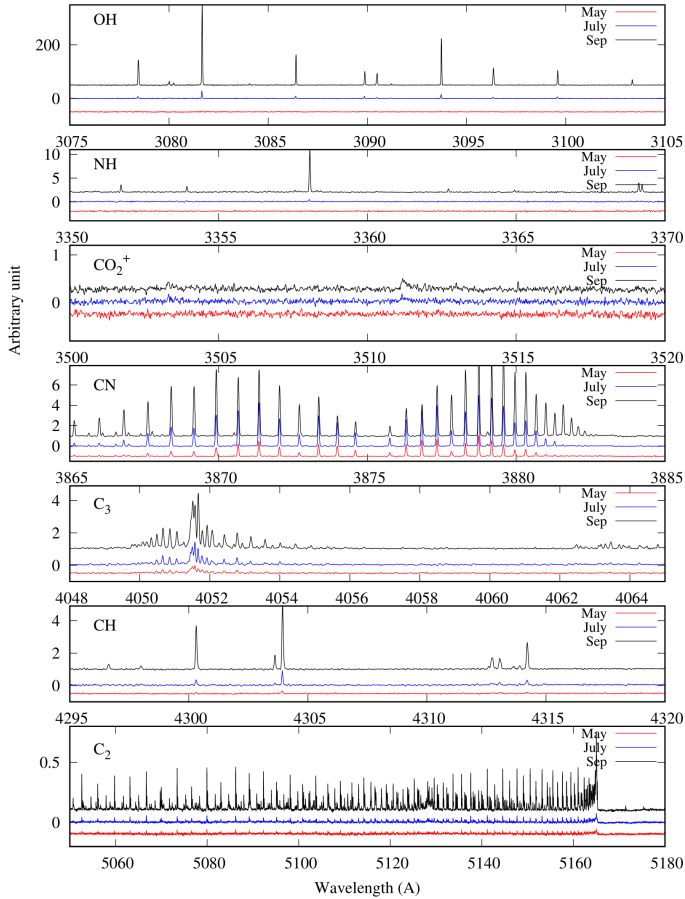


Fig. 8: Spectral regions of interest of comet C/2017 K2 acquired with UVES, with detected daughter species in three different epochs: May ($r_h=3.23$ au), July ($r_h=2.73$ au), and September ($r_h=2.12$ au). The flux is reported in arbitrary units for better display.

The production rates of these daughter species have been derived from a Haser model (Haser 1957) using the main emission bands (Table 7) and compared to expected parent species detected with CRRES⁺ simultaneously. The fluxes are, unfor-

tunately, too weak in CN lines to compute the N and C isotopic ratios.

Table 7: Gas production rates of comet C/2017 K2 from UVES observations

Date (2022)	OH	CN	C_2
May 09	$3.96 \pm 0.79 \times 10^{27}$	$7.57 \pm 1.51 \times 10^{25}$	$2.88 \pm 0.58 \times 10^{25}$
Jul 05 (a)	$1.23 \pm 0.12 \times 10^{28}$	$1.07 \pm 0.11 \times 10^{26}$	$7.03 \pm 1.41 \times 10^{25}$
Jul 05 (b)	$1.51 \pm 0.16 \times 10^{28}$	$1.15 \pm 0.12 \times 10^{26}$	$5.86 \pm 1.17 \times 10^{25}$
Sept 21	$5.23 \pm 0.51 \times 10^{28}$	$1.15 \pm 0.12 \times 10^{26}$	$1.01 \pm 0.20 \times 10^{26}$
Sept 22	$5.59 \pm 0.57 \times 10^{28}$	$1.18 \pm 0.11 \times 10^{26}$	$9.59 \pm 1.92 \times 10^{25}$

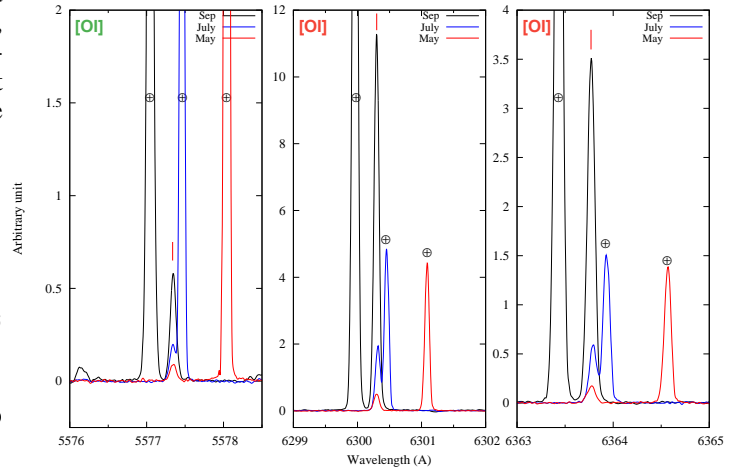


Fig. 9: The green forbidden oxygen line [OI] and the red doublet lines detected with UVES at the VLT on the 3 epochs: May 9 ($r_h=3.23$ au), July 5 ($r_h=2.73$ au), and Sept 20 ($r_h=2.12$ au)

The high resolution and sensitivity of UVES allowed us to detect at each epoch the three [OI] oxygen forbidden lines, the green one at 5577.31 Å and the red doublet at 6300.31 Å and at 6363.78 Å. Due to the Doppler shift caused by the comet's velocity with respect to the Earth, the comet lines are well separated from the strong telluric [OI] lines (see Figure 9). The flux measurements of each line and the so-called green-to-red ratio $G/R = I_{5577} / (I_{6300} + I_{6364})$ (Cochran & Cochran 2001) are reported for each epoch in Table 8. We observe a clear trend of the ratio with the heliocentric distance from a rather large value of 0.25 above the water sublimation line at 3.0 au (Crovissier & Encrenaz 2000) down to a value close to 0.1 at 2 au, in excellent agreement with the values reported by Decock et al. (2013),

Table 8: Flux measurements and G/R intensity ratios of [OI] emission lines for comet C/2017 K2.

Date (2022)	Fluxes [erg/s/cm ² /Å/arcsec ²]			G/R
	(5577 Å)	(6300 Å)	(6363 Å)	
May 09	1.64×10^{-17}	5.76×10^{-17}	1.98×10^{-17}	0.25 ± 0.013
Jul 05a	2.42×10^{-17}	1.52×10^{-16}	4.65×10^{-17}	0.14 ± 0.007
Jul 05b	4.03×10^{-17}	2.43×10^{-16}	7.43×10^{-17}	0.15 ± 0.008
Sept 21	1.01×10^{-16}	1.18×10^{-15}	3.82×10^{-16}	0.08 ± 0.004
Sept 22	1.02×10^{-16}	1.17×10^{-15}	3.62×10^{-16}	0.08 ± 0.005

and references therein with the addition of [Opitom et al. \(2019\)](#), [Cambianica et al. \(2021\)](#), [Cambianica et al. \(2023\)](#), [Kwon et al. \(2023\)](#) and [Aravind et al. \(2024\)](#), for comets observed at various heliocentric distances (see Figure 10). This ratio has been commonly used to determine the main parent molecule of the oxygen atoms in the coma, and particularly the relative contribution of the main comet activity drivers' H_2O , CO_2 , and CO , as oxygen is mainly produced by the photodissociation of those species ([Festou & Feldman 1981](#)). The G/R ratio depends indeed on the progenitor, as shown in Table 2 of [Festou & Feldman \(1981\)](#), with a value of 0.1 for water and higher values for CO and CO_2 . Sub-millimeter observations later confirmed the presence of carbon monoxide (CO) in K2's coma ([Yang et al. 2021](#)), and [Cambianica et al. \(2023\)](#) measured a high G/R ratio of 0.28 at 2.8 au. We found a large G/R of 0.25 at 3.2 au but a lower value of 0.15 at 2.7 au, in good agreement with the average value of 0.15 at 2.53 au from [Kwon et al. \(2023\)](#), using MUSE at the VLT. It then rapidly drops down to 0.08 at 2.1 au, in agreement with the trend of [Decock et al. \(2013\)](#). This illustrates the quick rise of water sublimation below 3.0 au, confirmed by the UVES data not showing OH lines, a photodissociation product of H_2O , until the second epoch. As this G/R trend is followed by several comets at large distances, including K2, we cannot then argue it was especially rich in CO or CO_2 compared to others, as an even larger ratio should have been found. The nondetection of CO and the detection of CO_2^+ might point to CO_2 to be the main contributor at larger heliocentric distances than 2.5 au. It would have been, of course, very interesting to obtain also the ratio at even larger distances than 4.0 au to test this hypothesis.

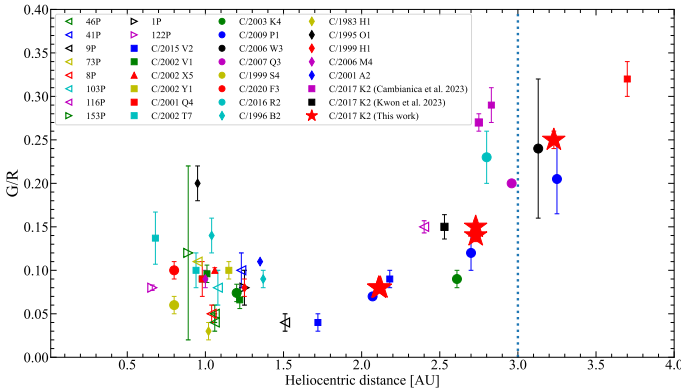


Fig. 10: The G/R intensity ratio plotted as a function of the heliocentric distance. The same symbol is used for multiple points of a given comet. Open markers represent short-period comets, and solid markers represent LPCs. The vertical dotted line indicates the distance beyond which water sublimation decreases significantly ([Crovisier & Encrenaz 2000](#)).

A recent and surprising discovery was the ubiquitous presence of neutral metallic lines of iron and nickel in high-resolution spectra of comets and detected even far from the Sun ([Manfroid et al. 2021](#)). In comet K2, we were able to identify and measure the flux of eight nickel lines and two iron lines in the blue spectra of the last two epochs, sometimes with large uncertainties (see Figure 11 and Table 9). We computed the iron and nickel production rates for the last two epochs: $\log_{10}(Q_{\text{Fe}}) = 22.01 \pm 0.21$ (July) and 22.14 ± 0.21 (Sept) and $\log_{10}(Q_{\text{Ni}}) = 21.97 \pm 0.04$ (July), and 22.23 ± 0.08 (Sept) using the same model developed in [Manfroid et al. \(2021\)](#) and [Hutsemékers et al. \(2021\)](#). The ratios for each epochs are then $\log_{10}(Q_{\text{Ni/Fe}}) = -0.04 \pm 0.22$ (July) and 0.09 ± 0.23 (Sept). They are in good

agreement within the error bars with the average value for 17 comets of $\log_{10}(Q_{\text{Ni/Fe}}) = -0.06 \pm 0.31$, but differs by one order of magnitude from the ratio of -1.10 ± 0.23 estimated in the dust of 1P/Halley ([Jessberger et al. 1988](#)) and -1.11 ± 0.09 measured in the coma of the Sun-grazing comet Ikeya-Seki by [Manfroid et al. \(2021\)](#). Despite being a DNC and active very far from the Sun, the ratio of Ni/Fe in K2 is similar to that of other comets. As shown in Figure 12, K2 falls in the middle of the correlation found by [Hutsemékers et al. \(2021\)](#) between the level of Carbon-chain depletion (C_2/CN) and the Ni/FeI ratio, of the LPC. The existence of this relation suggests that the diversity of Ni/FeI abundance ratios in comets could be related to the cometary formation rather than to subsequent processes in the coma.

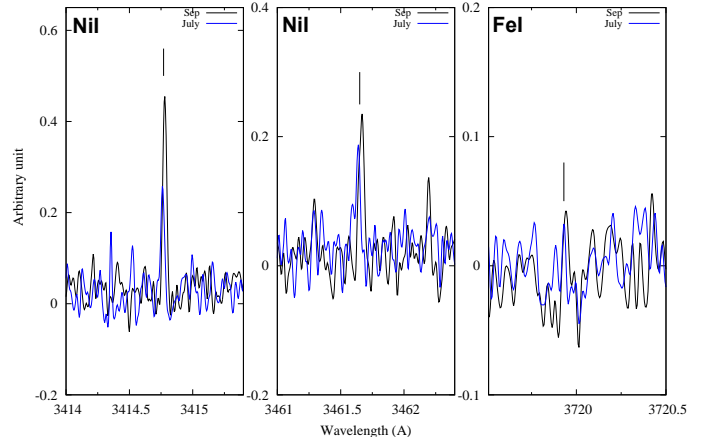


Fig. 11: Example of NiI and FeI lines detected in C/2017 K2.

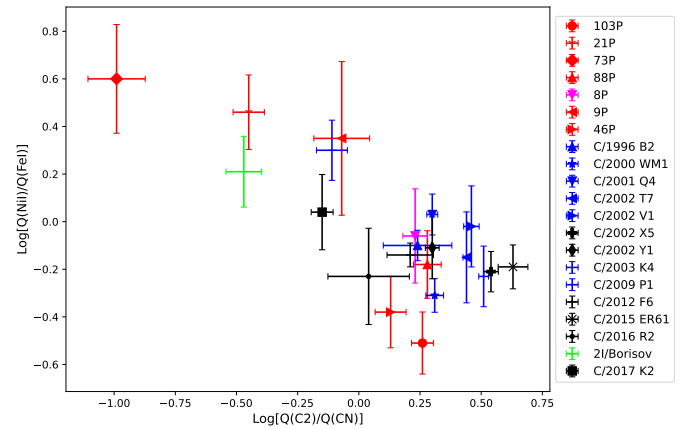


Fig. 12: NiI/FeI abundance ratios against the C_2/CN adapted from [Hutsemékers et al. \(2021\)](#). The colors in the plot represent different dynamical classes: Jupiter-family comets (red), Halley-family comets (pink), long-period comets (blue), and dynamically new comets (black), with a square symbol for comet C/2017 K2.

3.2.2. NIR spectroscopy with CRIRES⁺

The overall retrieved rotational temperatures, production rates, and mixing ratios (or significant upper limits) obtained from CRIRES⁺ spectra are reported in Table 11.

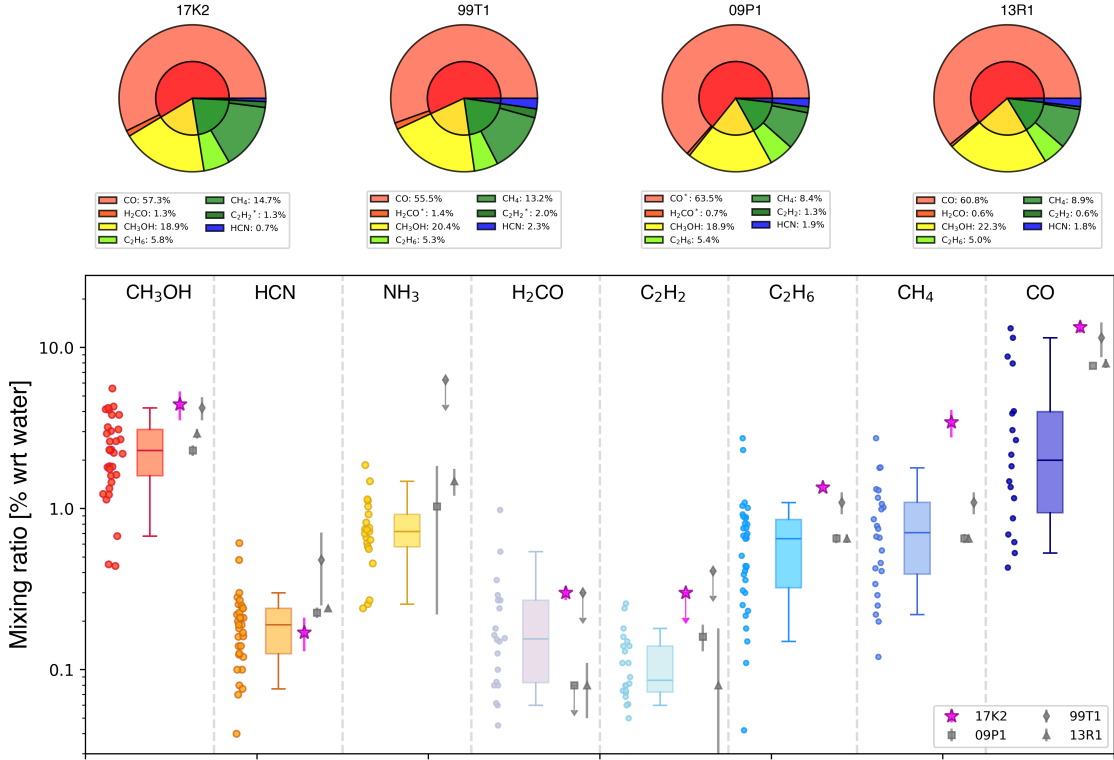


Fig. 13: Comparison of K2 with other comets. In the upper panel, the comet is compared with C/2009 P1, C/1999 T1, and C/2013 R1, which show the closest relative abundance proportions. In the bottom plot, for each molecular species, we compare K2 (marked with a magenta star) with the box plot statistic from other infrared results relative to comets observed within 2 au from the Sun (Lippi et al. 2021). For each box, the middle line corresponds to the median, the box limits to the 25th and 75th percentiles, and the whiskers to the 5th and 95th percentiles. C/2009 P1, C/1999 T1, and C/2013 R1 are also shown with a gray square, diamond, and triangle, respectively.

Table 9: Fluxes of NiI and FeI in C/2017 K2.

Line (Å)	July 5 (a)	Fluxes $\times 10^{-3}$ [erg/s/cm ² /Å/arcsec ²]		
		July 5 (b)	September 21	September 22
NiI 3414.764	8.0 \pm 3.0	10.0 \pm 3.0	10.0 \pm 3.0	17.0 \pm 3.0
NiI 3446.259	—	4.4 \pm 2.0	3.0 \pm 2.0	4.7 \pm 3.0
NiI 3458.460	—	—	—	20.0 \pm 10.0
NiI 3461.652	5.0 \pm 2.0	5.0 \pm 2.0	—	13.0 \pm 3.0
NiI 3492.956	—	—	6.0 \pm 3.0	—
NiI 3515.052	3.0 \pm 2.0	5.0 \pm 4.0	7.9 \pm 3.0	11.0 \pm 3.0
NiI 3524.536	6.0 \pm 2.0	10.0 \pm 3.0	13.7 \pm 3.0	15.0 \pm 3.0
NiI 3619.391	4.5 \pm 2.0	3.4 \pm 2.0	6.2 \pm 3.0	2.9 \pm 2.0
FeI 3719.935	—	3.9 \pm 2.0	—	4.9 \pm 2.0
FeI 3737.132	—	1.9 \pm 2.0	—	3.1 \pm 2.0

Despite the comet's notable activity even at large heliocentric distances, our infrared observations of K2 reveal a contrasting scenario, characterized by a very weak dust continuum and faint emission lines from many parent species. Because the dust signal in the infrared is a combination of reflected light and thermal emission, the low dust signal we see in our IR spectra could be attributed to the dust being cold since K2 was still quite far away from the Sun, combined with the dust properties (size, composition, etc.). Additional simulations are required to properly explain the differences observed between the optical and the infrared. Considering the volatile component, the infrared counterparts of optically detected species, such as H₂O, C₂H₂ and HCN, were barely discernible, even when the comet appeared bright. This is particularly evident in the spectra taken on May 9, where CO emission lines are at the noise level and too faint to allow a proper estimate of the production rate. In the begin-

ning, given the strong activity observed in the optical, we were expecting spectra dominated by hyper-volatiles such as CO and CH₄. Since this was not the case, we assumed that the comet was still too far from the Sun and the observer to be properly sampled in the infrared. Our later analysis and comparison with TRAPPIST and UVES results confirm instead a more complex scenario, where most likely our non-detection could be related to a near-surface depletion of CO before the comet entered the water ice-line ($r_h < 2.8$ au).

In Table 12, we compare our results with recent literature outcomes. Our total production rates and mixing ratios are comparable within 2σ with those obtained by Ejeta et al. (2025), with the exception of HCN, for which we get a significantly smaller value. Similarly, our production rates measured in July are consistent with those measured by the James Webb Space Telescope (JWST) when the comet was at 2.35 au from the Sun (Woodward et al. 2025), even if the latter report a water production rate two times larger than the one we measured, and consequently smaller mixing ratios.

When compared to other comets, K2 is enriched in almost all the species, and similar to C/1999 T1, C/2009 P1, and C/2013 R1 (see Figure 13). A possible scenario that can explain this composition is that the material in this comet formed in a cold, organic-rich environment, where CO was particularly abundant and hydrogenation processes on grains contributed significantly to the abundances of species such as methanol, ethane, and methane. Moreover, as a dynamically new comet, K2 most likely pre-

Table 10: Abundance ratios derived from the optical and infrared data of comet C/2017 K2

UT Date	r_h (au)	r_Δ (au)	Abundances ratios (10^{-3})					Tel/Instrument
			CN/OH	HCN/H ₂ O	C ₂ /OH	C ₂ H ₂ /H ₂ O	C ₂ H ₆ /H ₂ O	
2022 Jul 05	2.73	1.82	—	<3.88	—	<4.78	7.73±2.93	CRIRES ⁺
2022 Jul 07	2.71	1.82	5.56±3.89	—	5.98±4.18	—	—	TRAPPIST
2022 Sep 21	2.12	2.34	1.68±0.22	1.48±0.58	1.76±0.23	<3.14	13.30±3.20	TRAPPIST & CRIRES ⁺
2022 Sep 22	2.11	2.35	2.03±0.29	2.29±1.07	1.69±0.24	<4.93	14.50±3.50	TRAPPIST & CRIRES ⁺

Table 11: Production rates, and Mixing Ratios (MR, relative to water) retrieved for CRIRES⁺ observations

Date	Molecule	Q_{NC} [10^{26} mol/s]	$Q_{Tot}^{(a)}$ [10^{26} mol/s]	MR [% wrw]
5 July 2022	H ₂ O	203 ± 53	335 ± 96	100
	HCN	< 0.8	< 1.3	< 0.4
	C ₂ H ₂	< 0.9	< 1.5	< 0.5
	C ₂ H ₆	1.57 ± 0.34	2.59 ± 0.64	0.77 ± 0.32
	CH ₄	7.8 ± 1.7	12.9 ± 3.2	3.8 ± 0.8
	CO	21.8 ± 5.5	36 ± 10	10.7 ± 2.7
21 Sep 2022	H ₂ O ^(b)	252 ± 29	446 ± 82	100
	CH ₃ OH	10.5 ± 3.5	19 ± 7	4.2 ± 1.4
	HCN	0.37 ± 0.12	0.66 ± 0.23	0.15 ± 0.05
	C ₂ H ₂	< 0.8	< 1.4	< 0.3
	C ₂ H ₆	3.36 ± 0.22	5.95 ± 0.92	1.33 ± 0.09
	CH ₄ ^(b)	6.5 ± 3	11 ± 5	2.6 ± 1.2
	CO	35 ± 3	60 ± 10	13.9 ± 1.2
22 Sep 2022	H ₂ O ^(b)	252 ± 29	446 ± 82	100
	CH ₃ OH	11.5 ± 3.5	20 ± 6	4.6 ± 1.2
	HCN	0.58 ± 0.24	1.02 ± 0.44	0.23 ± 0.10
	C ₂ H ₂	< 1.2	< 2.2	< 0.5
	C ₂ H ₆	3.64 ± 0.26	6.45 ± 1.02	1.44 ± 0.10
	CH ₄ ^(b)	6.5 ± 3	11 ± 5	2.6 ± 1.2

Note: (a) Calculated using a Q_{scale} value of (1.65 ± 0.20), and (1.77 ± 0.25), for the July and September observations, respectively; (b) Weighted average of the two observations in September.

Table 12: Comparison of total production rates and mixing ratios as retrieved from this work, Ejeta et al. (2025) and Woodward et al. (2025).

r_h [au]	CRIRES ⁺		iSHELL	JWST
	2.7	2.1	2.35	2.35
Total Production Rates [10^{26} mol/s]				
H ₂ O	335 ± 96	446 ± 82	365 ± 66	760 ± 15
CH ₃ OH		19 ± 7	17.1 ± 1.9	22.2 ± 0.7
HCN	< 1.3	0.7 ± 0.2	1.75 ± 0.16	1.7 ± 0.3
C ₂ H ₂	< 1.5	< 1.4	1.97 ± 0.34	
C ₂ H ₆	2.6 ± 0.6	6.3 ± 0.9	5.25 ± 0.67	2.3 ± 0.4
CH ₄	12.9 ± 3.2	11.0 ± 5.0	15.7 ± 2.3	14.8 ± 0.4
CO	36 ± 10	60 ± 10	63.7 ± 5.7	62 ± 1
Mixing Ratios [w.r.t. water]				
CH ₃ OH		4.4 ± 1.2	4.69 ± 1	2.93 ± 0.08
HCN	< 0.4	0.2 ± 0.1	0.48 ± 0.10	0.23 ± 0.05
C ₂ H ₂	< 0.5	< 0.5	0.54 ± 0.13	
C ₂ H ₆	0.77 ± 0.32	1.4 ± 0.1	1.44 ± 0.32	0.31 ± 0.04
CH ₄	3.8 ± 0.8	2.6 ± 1.2	4.29 ± 1.0	1.95 ± 0.05
CO	10.7 ± 2.7	13.9 ± 1.2	17.5 ± 3.5	8.2 ± 0.3

served its primordial composition during its storage in the Oort cloud. This pristine and hyper-volatile material has enabled its strong activity even at heliocentric distances larger than 20 au.

3.3. Parent and daughter molecules

To investigate the origin of the radicals observed in the coma of K2, we compared the abundances of the daughter species with the parent molecular species derived from infrared observations using CRIRES⁺. Table 10 summarizes the abundances of selected radicals observed in the optical and their potential parent species detected in the infrared during the same period. Our CN/OH ratios align with the HCN/H₂O ratios obtained from the infrared observations on approximately the same dates, particularly on September 21, 2022 (see Table 10). This indicates that HCN is the primary source of observed CN. The significantly lower C₂ abundance compared to C₂H₆ suggests that C₂ is more likely to be dissociated from C₂H₂ than from C₂H₆. Previous studies have shown that C₂ remains associated with both molecules even at large heliocentric distances, as observed in comet Hale-Bopp (Helbert et al. 2005). Furthermore, no clear parent molecule for C₃ has been identified in the K2 infrared spectra, suggesting that C₃ may be produced by chemical reactions within the coma.

4. Summary and conclusion

In this study, we conducted a comprehensive observational analysis of comet C/2017 K2 (PanSTARRS), a Dynamically New Oort cloud comet that exhibited activity at a large heliocentric distance. Using data from the TRAPPIST telescopes, UVES, and CRIRES⁺ at the VLT, we characterized the long-term evolution of activity and molecular abundances across multiple wavelengths, while the comet was getting closer to the Sun. Our TRAPPIST photometric monitoring campaign spanned nearly eight years, covering the comet's approach to perihelion and its post-perihelion activity. Over 271 nights of observation, we acquired more than 2204 broad-band and 174 narrow-band images, providing an extensive dataset to analyze the comet's brightness variations and coma properties. The light curve revealed a steady evolution without significant outbursts, and the observed colors remained about the same over a wide range of heliocentric distances.

The narrow-band photometric data from TRAPPIST and spectroscopic data obtained from UVES and CRIRES⁺ allowed us to investigate the gas production rates and molecular composition of the coma. CN and C₂ radicals were first detected in March 2022, with subsequent detections of other species as the comet moved inward. Production rates exhibited a gradual increase before perihelion, followed by a stabilization phase. The analysis of relative molecular abundances, based on the ratios of C₂ and C₃ to CN and OH, classified K2 as a "typical" comet, consistent with the taxonomic classification of A'Hearn et al. (1995). Fur-

thermore, our comparison of parent and daughter species confirmed that HCN is the main source of CN, while C_2 is likely to be dissociated from C_2H_2 rather than C_2H_6 .

Our findings show that cometary colors do not provide a clear distinction between different dynamical classes, consistent with recent findings by Holt et al. (2024). Notably, comet K2 lies on the bluer end of the color distribution. The temporal evolution of its activity reveals distinct phases linked to the sublimation and exhaustion of the surface of various ices. Our analysis of the variation in absolute magnitude, $A(0)f_0$ and dust production highlighted a peculiar drop in the brightness and dust production between -260 and -170 days of perihelion. This may indicate variations in the sublimation mechanisms of CO and CO_2 relative to H_2O . The observed trends suggest that the temporary stall in activity was due to the depletion of hypervolatiles in the near-surface layers, with activity resuming as water sublimation became dominant near perihelion. The switch from a CO_2 domination to an H_2O dominated coma is also clear from the fast drop in the observed G/R ratio as the comet crossed the water ice sublimation line at ~ 3 au.

In general, our results provide valuable insight into the long-term evolution of comet K2 and its activity. The findings reinforce the idea that CO and other super-volatile species play a significant role in driving cometary activity at large heliocentric distances. In addition, the compositional characteristics of the comet contribute to a broader understanding of Dynamically New comets and their evolutionary pathways. Furthermore, our study suggests a possible depletion of the outer layers rich in super-volatiles, leading to noticeable changes in the volatile-driven activity as the comet approached the Sun. The existence of a class of comets experiencing progressive depletion of the outermost volatile-rich layers of the nucleus, resulting in fading of activity, will be further investigated in future works. Future observations of similar objects will help refine our understanding of the formation conditions and dynamical history of long-period comets.

Acknowledgements. This publication uses data products from the TRAPPIST project, under the scientific direction of Emmanuel Jehin, Director of Research at the Belgian National Fund for Scientific Research (F.R.S.-FNRS). TRAPPIST-South is funded by F.R.S.-FNRS under grant PDR T.0120.21, and TRAPPIST-North is funded by the University of Liège in collaboration with Cadi Ayyad University of Marrakech. CRIRES⁺ and UVES results are based on observations under the program 109.23GX, at the European Southern Observatory, Cerro Paranal. S. Hmiedouch acknowledges funding from the Belgian Academy for Research and Higher Education (ARES). M. Lippi acknowledges funding from the “NextGenerationEU” program, in the context of the Italian “Piano Nazionale di Ripresa e Resilienza (PNRR)”, project code SOE_0000188. M. Vander Donckt acknowledges support from the French-speaking Community of Belgium through its FRiA grant. The authors thank NASA, David Schleicher, and the Lowell Observatory for the loan of a set of HB comet filters.

References

A’Hearn, M. F. 1982, in IAU Colloq. 61: Comet Discoveries, Statistics, and Observational Selection, ed. L. L. Wilkening, 433–460
A’Hearn, M. F., Millis, R. C., Schleicher, D. O., Osip, D. J., & Birch, P. V. 1995, *Icarus*, 118, 223
A’Hearn, M. F., Schleicher, D. G., Millis, R. L., Feldman, P. D., & Thompson, D. T. 1984, *The Astronomical Journal*, 89, 579
Aravind, K., Venkataramani, K., Ganesh, S., et al. 2024, *MNRAS*, 530, 393
Ballester, P., Modigliani, A., Boitquin, O., et al. 2000, *The Messenger*, 101, 31
Bessell, M. S. 1990, *PASP*, 102, 1181
Bonev, B. P. 2005, PhD thesis, University of Toledo, Ohio
Cambianica, P., Cremonese, G., Munaretto, G., et al. 2021, *A&A*, 656, A160
Cambianica, P., Munaretto, G., Cremonese, G., et al. 2023, *A&A*, 674, L14
Cochran, A. L. & Cochran, W. D. 2001, *Icarus*, 154, 381

Combi, M., Mäkinen, T., Bertaux, J.-L., Quemerais, E., & Ferron, S. 2025, arXiv e-prints, arXiv:2505.11699
Crovisier, J. & Encrenaz, T., eds. 2000, *Comet science : the study of remnants from the birth of the solar system*
Decock, A., Jehin, E., Hutsemékers, D., & Manfroid, J. 2013, *A&A*, 555, A34
Divine, N. 1981, in *ESA Special Publication*, Vol. 174, *The Comet Halley. Dust and Gas Environment*, ed. B. Battrock & E. Swallow
Dorn, R. J., Anglada-Escude, G., Baade, D., et al. 2014, *The Messenger*, 156, 7
Ejeta, C., Gibb, E., DiSanti, M. A., et al. 2025, *AJ*, 169, 102
Farnham, T. L., Schleicher, D. G., & A’Hearn, M. F. 2000, *Icarus*, 147, 180
Festou, M. & Feldman, P. D. 1981, *A&A*, 103, 154
Gomes, R., Levison, H. F., Tsiganis, K., & Morbidelli, A. 2005, *Nature*, 435, 466
Hanner, M. S. & Newburn, R. L. 1989, *AJ*, 97, 254
Haser, L. 1957, *Bulletin de la Société Royale des Sciences de Liège*, 43, 740
Helbert, J., Rauer, H., Boice, D. C., & Huebner, W. F. 2005, *A&A*, 442, 1107
Hmiedouch, S., Jehin, E., Jabiri, A., et al. 2024, in *European Planetary Science Congress*, EPSC2024–1139
Holmberg, J., Flynn, C., & Portinari, L. 2006, *MNRAS*, 367, 449
Holt, C. E., Knight, M. M., Kelley, M. S. P., et al. 2024, *PSJ*, 5, 273
Hui, M.-T., Jewitt, D., & Clark, D. 2018, *AJ*, 155, 25
Hutsemékers, D., Manfroid, J., Jehin, E., Opatom, C., & Moulane, Y. 2021, *A&A*, 652, L1
Jehin, E., Gillon, M., Queloz, D., et al. 2011, *The Messenger*, 145, 2
Jessberger, E. K., Christoforidis, A., & Kissel, J. 1988, *Nature*, 332, 691
Jewitt, D. 2015, *AJ*, 150, 201
Jewitt, D., Agarwal, J., Hui, M.-T., et al. 2019, *AJ*, 157, 65
Jewitt, D., Hui, M.-T., Mutchler, M., et al. 2017, *ApJ*, 847, L19
Jones, G. H., Snodgrass, C., Tubiana, C., et al. 2024, *Space Sci. Rev.*, 220, 9
Kaeufli, H.-U., Ballester, P., Biereichel, P., et al. 2004, in *Society of Photo-Optical Instrumentation Engineers (SPIE) Conference Series*, Vol. 5492, *Ground-based Instrumentation for Astronomy*, ed. A. F. M. Moorwood & M. Iye, 1218–1227
Kaiser, N. & Pan-STARRS Team. 2002, in *American Astronomical Society Meeting Abstracts*, Vol. 201, *American Astronomical Society Meeting Abstracts*, 122.07
Królikowska, M. & Dybczyński, P. A. 2018, *A&A*, 615, A170
Kwon, Y. G., Bagnulo, S., Markkanen, J., et al. 2024, *AJ*, 168, 164
Kwon, Y. G., Opatom, C., & Lippi, M. 2023, *A&A*, 674, A206
Lippi, M., Vander Donckt, M., Faggi, S., et al. 2023, *A&A*, 676, A105
Lippi, M., Villanueva, G. L., Mumma, M. J., et al. 2020, *AJ*, 159, 157
Lippi, M., Villanueva, G. L., Mumma, M. J., & Faggi, S. 2021, *AJ*, 162, 74
Liu, B. & Liu, X. 2024, *A&A*, 683, A51
Manfroid, J., Hutsemékers, D., & Jehin, E. 2021, *Nature*, 593, 372
Marcus, J. N. 2007, *International Comet Quarterly*, 29, 39
Masci, F. J., Laher, R. R., Rusholme, B., et al. 2019, *PASP*, 131, 018003
Meech, K. J., Kleyna, J. T., Hainaut, O., et al. 2017, *ApJ*, 849, L8
Meier, R., Wellnitz, D., Kim, S. J., & A’Hearn, M. F. 1998, *Icarus*, 136, 268
Morbidelli, A., Tsiganis, K., Crida, A., Levison, H. F., & Gomes, R. 2007, *The Astronomical Journal*, 134, 1790
Moulane, Y., Jehin, E., Opatom, C., et al. 2018, *A&A*, 619, A156
Opatom, C., Hutsemékers, D., Jehin, E., et al. 2019, *A&A*, 624, A64
Opatom, C., Jehin, E., Manfroid, J., et al. 2015, *Astronomy & Astrophysics*, 574, A38
Paufigue, J., Biereichel, P., Donaldson, R., et al. 2004, in *Society of Photo-Optical Instrumentation Engineers (SPIE) Conference Series*, Vol. 5490, *Advancements in Adaptive Optics*, ed. D. Bonaccini Calia, B. L. Ellerbroek, & R. Ragazzoni, 216–227
Radeva, Y. L., Mumma, M. J., Villanueva, G. L., & A’Hearn, M. F. 2011, *ApJ*, 729, 135
Schleicher, D. G. 2010, *AJ*, 140, 973
Schleicher, D. G. & A’Hearn, M. F. 1988, *ApJ*, 331, 1058
Schleicher, D. G., Millis, R. L., & Birch, P. V. 1998, *Icarus*, 132, 397
Villanueva, G. L., Liuzzi, G., Faggi, S., et al. 2022, *Fundamentals of the Planetary Spectrum Generator*
Villanueva, G. L., Mumma, M. J., Bonev, B. P., et al. 2012, *J. Quant. Spec. Radiat. Transf.*, 113, 202
Villanueva, G. L., Mumma, M. J., DiSanti, M. A., et al. 2011, *Icarus*, 216, 227
Villanueva, G. L., Smith, M. D., Protapapa, S., Faggi, S., & Mandell, A. M. 2018, *J. Quant. Spec. Radiat. Transf.*, 217, 86
Wainscoat, R. J., Wells, L., Micheli, M., & Sato, H. 2017, *Central Bureau Electronic Telegrams*, 4393, 1
Whipple, F. L. 1950, *ApJ*, 111, 375
Willmer, C. N. A. 2018, *ApJS*, 236, 47
Womack, M., Sarid, G., & Wierzbos, K. 2017, *PASP*, 129, 031001
Woodward, C. E., Bockelee-Morvan, D., Harker, D. E., et al. 2025, arXiv e-prints, arXiv:2504.19849
Yang, B., Jewitt, D., Zhao, Y., et al. 2021, *ApJ*, 914, L17
Zhang, Q., Kolokolova, L., Ye, Q., & Vissapragada, S. 2022, *PSJ*, 3, 135
Zhang, X. L., Jewitt, D., & Hui, M. T. 2019, *MNRAS*, 487, 2919

Appendix A: Gas production rates and $A(0)f_{\rho}$ parameter from TRAPPIST data.

Table A.1: Gas production rates and $A(0)f\rho$ parameter of comet C/2017 K2 (PanSTARRS) from TRAPPIST data. The $A(0)f\rho$ values are computed within a radius aperture of 5-arcsecond from the nucleus and corrected for the phase angle effect.

UT Date	r_h (au)	r_Δ (au)	OH	Production rates (molec/s)				$A(0)f\rho$ (cm)				
				NH	CN	C ₂	C ₃	BC	RC	GC	Rc	
2017-10-25	15.18	15.31										3773.40±717.30
2018-11-06	12.89	13.08										5986.88±562.23
2018-11-10	12.87	13.06										5123.75±409.26
2019-04-08	11.92	11.85										6809.18±249.87
2019-05-10	11.71	11.56										6739.79±212.81
2019-05-28	11.59	11.41										5911.20±256.14
2019-06-05	11.54	11.35										6225.22±323.87
2019-06-09	11.51	11.33										6903.24±222.92
2019-06-11	11.50	11.31										6693.24±260.36
2019-06-12	11.49	11.31										6121.04±248.04
2019-06-25	11.40	11.22										6826.96±204.70
2019-07-17	11.26	11.11										6489.91±617.77
2019-07-20	11.24	11.10										6881.36±577.68
2019-07-22	11.23	11.09										7358.43±375.48
2019-07-28	11.18	11.06										6669.67±230.02
2019-09-26	10.78	10.89										6730.76±249.43
2019-10-03	10.73	10.87										7157.57±260.69
2019-10-23	10.60	10.81										7109.72±207.93
2019-10-24	10.59	10.81										7260.67±229.85
2019-11-03	10.52	10.77										7110.86±293.56
2020-01-27	9.94	10.18										7385.39±256.92
2020-01-28	9.93	10.17										7304.06±318.19
2020-02-04	9.88	10.10										7118.60±203.10
2020-02-08	9.85	10.05										7101.09±340.09
2020-03-10	9.63	9.69										7832.26±762.57
2020-03-17	9.59	9.61										8064.85±252.32
2020-04-03	9.46	9.40										8108.65±182.73
2020-04-15	9.38	9.25										7519.40±263.56
2020-04-17	9.37	9.23										7946.26±147.37
2020-04-27	9.29	9.12										7994.35±167.97
2020-05-05	9.24	9.03										7308.59±207.45
2020-05-09	9.21	8.98										8162.83±220.96
2020-05-20	9.13	8.88										7793.10±152.64
2020-05-24	9.10	8.84										7740.78±120.90
2020-06-02	9.04	8.76										7714.21±143.66
2020-07-11	8.75	8.49										7550.97±249.67
2020-07-23	8.66	8.44										7506.43±89.91
2020-07-24	8.65	8.43										7793.29±122.18
2020-08-05	8.56	8.39										7863.07±265.63
2020-08-12	8.51	8.38										8013.76±95.72
2020-08-27	8.40	8.35										7692.02±154.72
2020-09-07	8.31	8.33										8771.15±99.06
2020-09-21	8.21	8.32										8503.51±204.74
2020-10-05	8.11	8.30										9216.04±115.88
2020-10-11	8.06	8.29										8868.92±173.21
2020-10-24	7.96	8.26										9022.92±161.57
2020-12-07	7.63	8.08										9439.39±324.59
2021-04-22	6.55	6.31										9637.61±234.19
2021-05-06	6.44	6.11										10034.74±118.95
2021-05-12	6.39	6.04										10363.67±80.99
2021-06-05	6.19	5.73										10333.07±63.64
2021-06-22	6.06	5.58										11414.00±106.92
2021-06-28	6.01	5.54										11205.46±98.23
2021-09-09	5.38	5.40										12457.29±87.67
2021-09-13	5.35	5.40										11995.34±99.31
2022-01-12	4.29	5.00										12140.12±176.53
2022-01-13	4.29	4.98										11988.58±175.16
2022-02-02	4.11	4.69										12096.66±113.28
2022-03-13	3.75	3.94										12256.02±102.55
2022-03-25	3.64	3.67										11632.88±185.45
2022-03-28	3.62	3.60			1.27±0.10e+26	1.49±0.25e+26						
2022-03-29	3.61	3.58										12237.24±268.79
2022-03-31	3.59	3.53			1.35±0.10e+26	1.22±0.51e+26						11261.88±285.32
2022-04-01	3.58	3.51										11879.42±130.81
2022-04-02	3.57	3.48										11398.86±87.10
2022-04-07	3.52	3.37			1.45±0.10e+26	9.69±1.33e+25						11291.50±128.80
2022-04-08	3.52	3.34			1.48±0.11e+26	1.57±0.18e+26						10897.88±218.57
2022-04-09	3.51	3.32			1.43±0.09e+26	1.61±0.26e+26	10399.28±181.51	12016.04±269.77				10996.01±284.99
2022-04-13	3.47	3.23			1.54±0.10e+26	1.05±0.40e+26	9684.19±186.76	11590.88±233.66	10186.83±169.10			10533.13±199.45
2022-04-27	3.34	2.90	1.66±2.67e+28		1.64±0.12e+26	1.17±0.18e+26	9196.37±150.20	11067.33±108.19	9736.40±106.83			10056.05±206.61

UT Date	r_h (au)	r_A (au)	Production rates (molec/s)					A(0) f_p (cm)			
			OH	NH	CN	C ₂	C ₃	BC	RC	GC	Rc
2022-04-28	3.33	2.88			1.65±0.17e+26	1.61±0.14e+26	4.43±0.42e+25	9538.22±159.89	11321.08±77.96	9914.76±81.62	10297.28±87.87
2022-05-03	3.29	2.77	1.55±2.75e+28		1.84±0.10e+26	1.25±0.19e+26		9519.65±189.15	10717.32±102.76	9706.76±193.03	10458.82±68.31
2022-05-10	3.23	2.61						9969.13±225.41	11222.31±75.99	9454.35±153.78	10208.94±64.32
2022-05-16	3.17	2.49	1.73±1.04e+28		1.78±0.17e+26	1.54±0.17e+26	4.41±0.46e+25	9421.87±273.13	10642.21±250.59	9352.73±263.42	10170.12±80.43
2022-05-24	3.10	2.33	1.71±2.54e+28				4.27±0.36e+25	9290.15±113.26	10757.36±62.29	9352.46±67.50	9896.96±80.55
2022-05-25	3.09	2.31	1.73±2.53e+28				2.96±0.23e+25				
2022-05-27	3.07	2.27			2.03±0.11e+26		3.25±0.56e+25	9504.32±144.52	10969.99±52.51	9427.29±98.70	9958.57±82.59
2022-06-08	2.97	2.08	1.77±0.85e+28				3.62±0.34e+25				
2022-06-09	2.96	2.06	1.82±0.76e+28		2.07±0.11e+26	1.66±0.11e+26	3.94±0.33e+25	8403.57±154.27	9984.15±56.12	8737.93±59.34	9257.98±45.74
2022-06-11	2.94	2.04									9622.98±55.25
2022-06-13	2.92	2.01	2.15±2.31e+28		2.09±0.10e+26	1.72±0.17e+26		8353.38±144.28	10330.02±77.70	9062.00±79.13	9644.26±73.33
2022-06-18	2.88	1.95	2.64±0.58e+28				3.93±0.23e+25				
2022-06-29	2.78	1.85	3.21±2.57e+28		1.98±0.10e+26		4.23±0.28e+25	8160.92±116.02	9976.38±98.02	8800.84±60.67	
2022-06-30	2.77	1.85			2.04±0.09e+26	2.08±0.11e+26	5.65±0.27e+25	8559.22±94.85	10329.01±59.58	8938.91±55.58	9485.21±32.65
2022-07-04	2.74	1.83			2.08±0.10e+26	2.14±0.10e+26	4.97±0.27e+25	8699.99±110.97	10578.42±42.53	9188.18±51.66	9424.96±37.03
2022-07-07	2.71	1.82	3.58±2.50e+28		1.99±0.09e+26				9760.89±41.91		
2022-08-17	2.37	2.00	6.70±0.65e+28	6.99±3.12e+25	2.08±0.09e+26	2.12±0.12e+26	4.63±0.35e+25	9354.06±234.69	11412.33±68.11		
2022-08-18	2.36	2.01	7.77±0.79e+28			2.08±0.10e+26	4.42±0.31e+25				
2022-08-19	2.35	2.02	6.39±0.62e+28	1.24±0.30e+26	1.98±0.06e+26	2.24±0.07e+26				9895.09±54.92	10516.60±66.31
2022-08-21	2.34	2.04	7.28±0.67e+28		1.76±0.05e+26						10293.35±33.15
2022-08-22	2.34	2.04						8756.62±79.16	11317.90±29.44	9474.49±46.04	
2022-08-23	2.33	2.05	7.76±0.79e+28		1.84±0.06e+26	1.74±0.07e+26	4.08±0.18e+25		11244.40±33.43	9495.22±56.85	10373.68±43.67
2022-08-24	2.32	2.06	7.72±0.80e+28		1.78±0.06e+26			9093.19±85.92	11494.16±38.14	9694.42±63.94	10489.86±60.71
2022-08-25	2.32	2.07	6.40±0.68e+28						11055.06±33.76		10541.86±33.13
2022-08-27	2.30	2.09	7.77±0.94e+28		1.97±0.07e+26	1.84±0.10e+26	4.29±0.22e+25	9108.89±101.31	11525.30±35.50	9624.97±77.85	10390.12±50.79
2022-08-29	2.29	2.11	7.92±0.89e+28	1.01±0.22e+26	1.94±0.07e+26	1.86±0.10e+26		8788.41±101.57	11209.29±39.64	9398.84±70.91	10404.27±55.99
2022-08-31	2.26	2.14	8.17±0.79e+28		1.89±0.07e+26						10404.26±40.15
2022-09-01	2.26	2.14	7.95±1.12e+28						11454.41±37.48	9470.84±56.70	10415.31±40.58
2022-09-02	2.26	2.15	9.08±1.12e+28		2.04±0.08e+26	1.84±0.12e+26	4.27±0.27e+25	8871.96±146.23	10985.71±72.02		10303.84±63.37
2022-09-04	2.23	2.18	8.42±0.80e+28		1.88±0.06e+26						10665.87±48.86
2022-09-05	2.23	2.18					3.68±0.22e+25	9060.62±111.16			
2022-09-06	2.23	2.19		1.64±0.53e+26	2.03±0.12e+26						
2022-09-10	2.20	2.23	9.13±1.08e+28		1.95±0.10e+26	1.55±0.10e+26	4.36±0.27e+25	9129.88±155.01	11443.29±41.76	9874.95±74.51	10462.40±60.76
2022-09-14	2.17	2.28	8.80±0.91e+28								10537.60±52.00
2022-09-15	2.17	2.28			1.83±0.07e+26	1.50±0.09e+26		9149.68±104.65	11114.51±49.07		
2022-09-18	2.14	2.32	7.96±0.97e+28	1.13±0.36e+26							
2022-09-19	2.14	2.32			1.74±0.07e+26	1.65±0.09e+26	4.02±0.23e+25	8613.29±137.74			
2022-09-20	2.12	2.33	9.26±1.18e+28	1.36±0.31e+26							
2022-09-21	2.12	2.34	1.03±0.13e+29	1.16±0.35e+26	1.73±0.07e+26	1.81±0.08e+26	3.46±0.23e+25	8778.92±125.11	11023.20±45.71		
2022-09-22	2.12	2.35			1.91±0.12e+26	1.59±0.09e+26	4.01±0.28e+25	9186.00±126.76	11420.02±53.39	9573.12±83.00	10765.38±66.64
2022-09-23	2.10	2.36	9.43±1.23e+28	1.17±0.30e+26							10721.47±59.64
2022-09-24	2.10	2.36			1.78±0.07e+26	1.82±0.08e+26	3.98±0.29e+25	9027.18±137.67	11104.90±71.01	9649.48±88.50	
2022-09-26	2.09	2.39	8.06±1.01e+28	3.39±0.26e+26							
2022-09-30	2.06	2.42	1.08±0.15e+29								10977.33±60.48
2022-10-01	2.06	2.43	1.11±0.16e+29		1.98±0.08e+26	2.23±0.10e+26	4.65±0.32e+25	8952.98±149.53	11829.10±73.71		11104.32±67.78
2022-10-02	2.06	2.43			1.98±0.08e+26	1.63±0.11e+26	4.34±0.34e+25	9257.92±157.17	11781.13±59.43		10995.86±77.05
2022-10-06	2.03	2.46	1.14±0.18e+29								11219.20±76.82
2022-10-07	2.03	2.46			2.04±0.09e+26	2.04±0.11e+26		9065.49±153.03	11713.52±60.41		
2022-10-12	1.99	2.50	1.08±0.18e+29								11120.46±101.29
2022-10-13	1.99	2.50			1.96±0.10e+26	1.98±0.12e+26		9798.04±194.68	11829.96±81.96		
2022-10-14	1.98	2.51	1.18±0.22e+29								
2022-10-15	1.98	2.52	1.20±0.23e+29		2.14±0.11e+26	2.13±0.13e+26		10377.08±197.29	12643.32±58.22		11639.50±130.00
2022-10-16	1.98	2.52			2.01±0.10e+26	2.25±0.13e+26		10272.49±197.62	12408.85±102.82		11470.76±96.15
2022-10-19	1.96	2.54	1.22±0.23e+29								
2022-10-20	1.95	2.54		3.09±0.61e+26	2.01±0.10e+26	2.01±0.11e+26					
2022-10-21	1.95	2.54				2.68±0.12e+26	5.67±0.37e+25				
2022-10-22	1.94	2.55		3.87±0.70e+26							
2022-10-23	1.94	2.56		4.18±0.73e+26		3.06±0.14e+26	6.21±0.41e+25				
2022-10-24	1.94	2.56				3.20±0.15e+26	6.19±0.42e+25				
2023-01-28	1.87	2.26	1.33±0.29e+29		2.84±0.14e+26	2.61±0.17e+26		13528.06±259.55	14924.44±63.84	13337.70±133.27	14127.19±102.92
2023-01-29	1.87	2.26	1.41±0.30e+29		2.82±0.14e+26		6.82±0.52e+25	13436.79±256.50			13814.90±98.71
2023-01-30	1.87	2.25	1.37±0.28e+29		2.69±0.13e+26		6.93±0.53e+25	13409.13±243.76			13484.26±95.29
2023-01-31	1.88	2.25	1.22±0.25e+29		2.60±0.13e+26		7.07±0.50e+25	12725.15±233.41			12759.80±88.69
2023-02-23	1.98	2.24	9.92±1.45e+28	1.69±0.38e+26	2.22±0.09e+26	2.18±0.10e+26	5.38±0.33e+25	10774.56±169.30	11938.66±40.10	10613.67±97.15	11343.67±70.31
2023-02-26	2.00	2.25	1.29±0.30e+29	3.57±0.78e+26	2.49±0.18e+26	2.32±0.15e+26					11419.44±67.93
2023-02-27	2.00	2.25					5.66±0.33e+25	11001.79±144.41	12708.20±46.60	10853.59±77.64	11854.54±66.27
2023-03-04	2.03	2.27	9.94±1.38e+28	2.43±0.51e+26	2.25±0.10e+26		5.40±0.41e+25	10955.75±186.81	11938.53±79.65	10635.30±116.84	11488.29±85.20
2023-03-13	2.09	2.34	7.16±0.99e+28								
2023-03-14	2.09	2.34		2.04±0.47e+26	2.22±0.09e+26	2.11±0.08e+26	5.58±0.33e+25	9935.40±159.32			11085.31±75.40
2023-03-20	2.13	2.40	7.10±0.96e+28	1.26±0.59e+26							
2023-03-21	2.13	2.40			2.06±0.09e+26	1.74±0.08e+26	4.89±0.30e+25	9539.89±176.97	10538.70±48.97	9343.81±84.38	
2023-03-23	2.15	2.43			2.19±0.10e+26						
2023-03-24	2.15	2.43				1.73±0.09e+26	5.55±0.33e+25	9418.33±122.62			10562.88±55.61
2023-03-26	2.18	2.46	7.83±1.11e+28								
2023-03-27	2.18	2.46			2.27±0.09e+26	1.74±0.10e+26	5.96±0.37e+25	9463.55±152.08		9645.06±89.73	

UT Date	r_h (au)	r_Δ (au)	OH	Production rates (molec/s)						A(0)f ρ (cm)		
				NH	CN	C ₂	C ₃	BC		RC	GC	Rc
2023-03-30	2.20	2.51	8.11±1.40e+28									
2023-03-31	2.20	2.51										
2023-04-10	2.28	2.65	3.87±0.73e+28	2.33±0.71e+26	2.30±0.10e+26	1.53±0.10e+26	5.49±0.44e+25					
2023-04-11	2.28	2.65			2.17±0.10e+26							
2023-04-18	2.34	2.76				1.56±0.10e+26		9781.91±176.84				
2023-04-19	2.35	2.77	5.33±1.21e+28		2.08±0.08e+26	1.32±0.10e+26	4.88±0.37e+25					9480.55±67.10
2023-04-26	2.41	2.88						10010.17±172.54	10451.85±54.06			10070.73±50.00
2023-04-28	2.42	2.91										9537.65±56.30
2023-04-29	2.43	2.92										10318.65±65.31
2023-05-03	2.46	2.98										9696.57±67.18
2023-05-07	2.49	3.04										9338.61±63.24
2023-08-25	3.46	3.92										9433.18±61.48
2023-09-16	3.65	3.84										9724.36±50.56
2023-09-20	3.69	3.82	3.51±53.70e+26		2.02±0.25e+25			6664.21±163.02	7101.00±83.87			9228.83±61.84
2023-09-24	3.73	3.80										7387.04±118.02
2023-09-25	3.73	3.80				1.02±0.15e+26		6782.46±262.86	7289.63±75.36			8428.02±56.18
2023-09-29	3.77	3.77										8787.31±45.49
2023-10-05	3.83	3.74			2.04±0.68e+25	8.78±1.94e+25	7.73±2.41e+24					8617.09±68.03
2023-10-06	3.84	3.73										7403.56±65.80
2023-10-08	3.85	3.72										7364.98±63.78
2023-10-10	3.87	3.71										7378.67±44.75
2023-10-11	3.88	3.70			2.97±0.37e+25							7505.57±65.87
2023-10-15	3.92	3.67										7077.14±77.66
2023-10-20	3.96	3.65										7178.48±41.37
2023-10-26	4.01	3.61						6313.46±150.46	6873.33±97.94			7523.33±36.77
2023-11-08	4.13	3.55										7180.85±76.53
2023-11-12	4.17	3.54										7308.62±52.94
2023-11-14	4.19	3.53										6716.60±64.68
2023-11-16	4.20	3.52										6694.86±53.90
2023-11-18	4.22	3.52										7426.78±85.88
2023-11-22	4.26	3.52										7480.30±69.18
2023-12-06	4.38	3.53										6906.71±50.66
2023-12-07	4.39	3.54										6947.59±36.70
2023-12-09	4.42	3.55										6187.96±49.97
2023-12-10	4.43	3.55										6828.59±55.06
2023-12-11	4.43	3.56										6934.24±62.69
2023-12-14	4.46	3.58										6101.98±89.04
2023-12-18	4.50	3.61										6812.69±66.66
2023-12-21	4.52	3.63										6726.98±60.82
2024-01-02	4.63	3.76										5994.54±55.49
2024-01-06	4.66	3.81										6460.88±51.61
2024-01-23	4.82	4.11										6656.26±31.48
2024-01-24	4.82	4.13										6503.41±73.57
2024-01-27	4.85	4.19										6291.64±77.35
2024-02-03	4.91	4.34										5967.72±59.84
2024-02-11	4.98	4.52										6087.57±51.16
2024-02-12	4.99	4.54										6413.08±93.37
2024-02-21	5.07	4.75										6198.75±54.54
2024-02-29	5.14	4.95										6251.93±117.50
2024-03-04	5.17	5.05										6261.90±73.92
2024-03-10	5.22	5.18										5418.19±66.65
2024-04-03	5.42	5.77										6076.09±40.21
2024-04-09	5.47	5.91										5622.44±51.66
2024-04-11	5.50	5.97										5344.47±67.99
2024-09-12	6.76	6.98										5408.12±103.88
2024-09-14	6.78	6.96										4619.09±156.38
2024-09-26	6.88	6.86										4548.82±178.25
2024-09-27	6.88	6.85										4648.64±189.65
2024-10-04	6.94	6.79										4745.24±197.46
2024-10-30	7.15	6.57										4517.08±81.08
2024-11-04	7.18	6.54										3865.80±56.82
2024-11-11	7.24	6.50										3705.50±143.13
2024-11-23	7.33	6.47										3125.83±130.47
2024-11-27	7.37	6.47										3807.00±95.94
2024-12-03	7.42	6.48										3051.94±107.26
2024-12-11	7.47	6.50										3737.69±112.79
2024-12-19	7.54	6.55										4024.36±201.05
2025-01-04	7.66	6.72										2846.36±237.66
2025-01-20	7.78	6.96										2718.69±127.23
2025-01-25	7.82	7.05										4196.35±114.38
2025-02-01	7.88	7.21										3892.18±190.63
2025-02-17	8.00	7.57										3880.53±219.32
2025-03-26	8.28	8.47										3693.66±117.04
2025-04-20	8.46	9.04										3475.26±262.88
												2680.62±329.86

Appendix B: Light curve, absolute magnitude evolution, and g-factors.

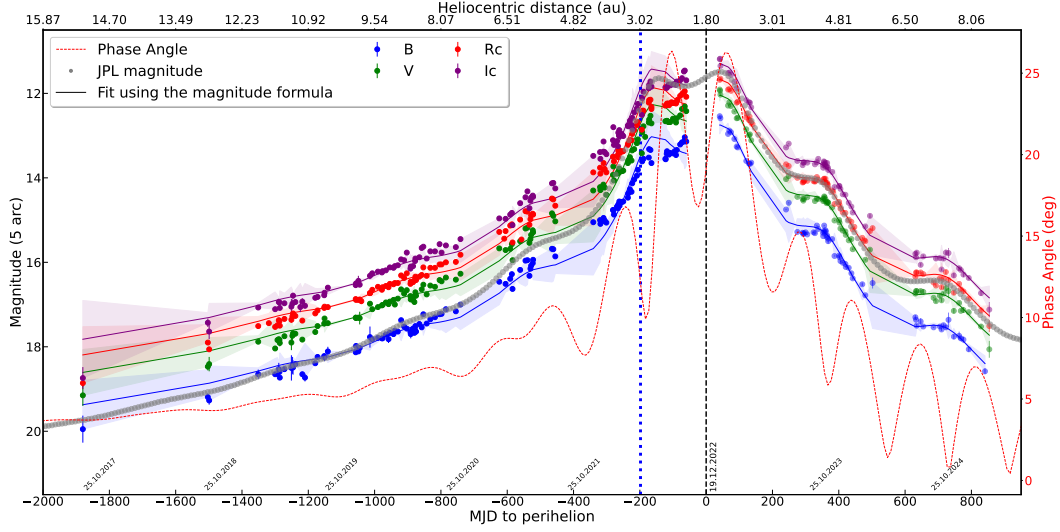


Fig. B.1: TRAPPIST Light curve of comet C/2017 K2 measured within a radius aperture of 5-arcseconds as a function of time and distance to perihelion. The vertical dashed line indicates the perihelion at 1.79 au on December 19, 2022. The vertical blue dotted line represents the water ice sublimation boundary (~ 3 au).

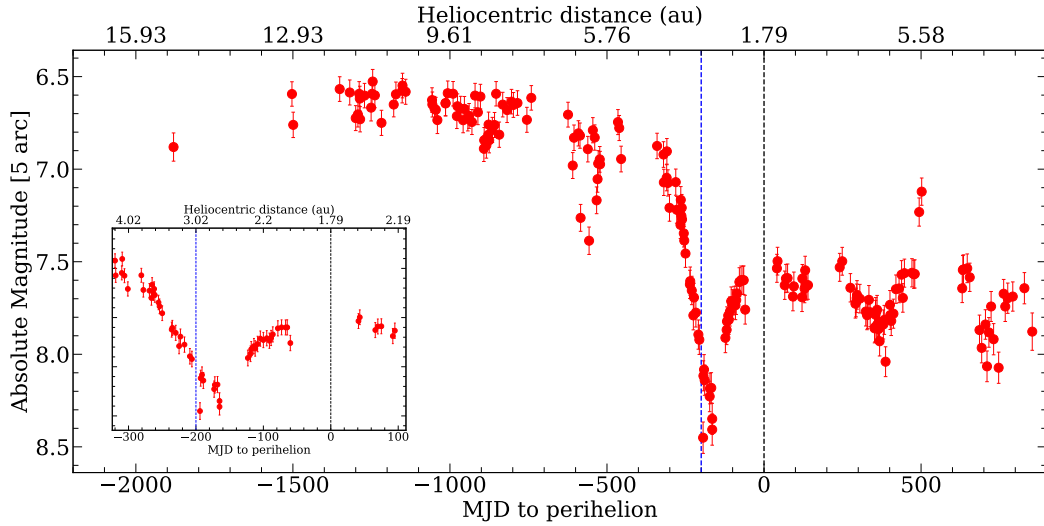


Fig. B.2: The absolute magnitude of comet C/2017 K2 as a function of days to perihelion. The vertical blue dotted line represents the water ice sublimation boundary (~ 3 au) (Womack et al. 2017; Crovisier & Encrenaz 2000), and the dashed line represents the perihelion. The inset is a zoomed-in region of the light curve around 3 au.

Table B.1: The scale lengths, lifetimes, and the fluorescence efficiencies of the different radicals at 1 au scaled by r_h^{-2} . The fluorescence efficiencies are taken from Schleicher's website.

Molecules	Parent (km)	Daughter (km)	Lifetime (s)	g-factors $\text{erg s}^{-1} \text{mol}^{-1}$
OH(0,0)	2.4×10^4	1.6×10^5	1.6×10^5	1.49×10^{-15}
NH(0,0)	5.0×10^4	1.5×10^5	1.3×10^4	6.27×10^{-14}
CN($\Delta v=0$)	1.3×10^4	2.1×10^5	2.1×10^5	2.62×10^{-13}
$\text{C}_3(\lambda=4050 \text{ \AA})$	2.8×10^3	2.7×10^5	2.7×10^5	1.00×10^{-12}
$\text{C}_2(\Delta v=0)$	2.2×10^4	6.6×10^4	6.6×10^4	4.50×10^{-13}

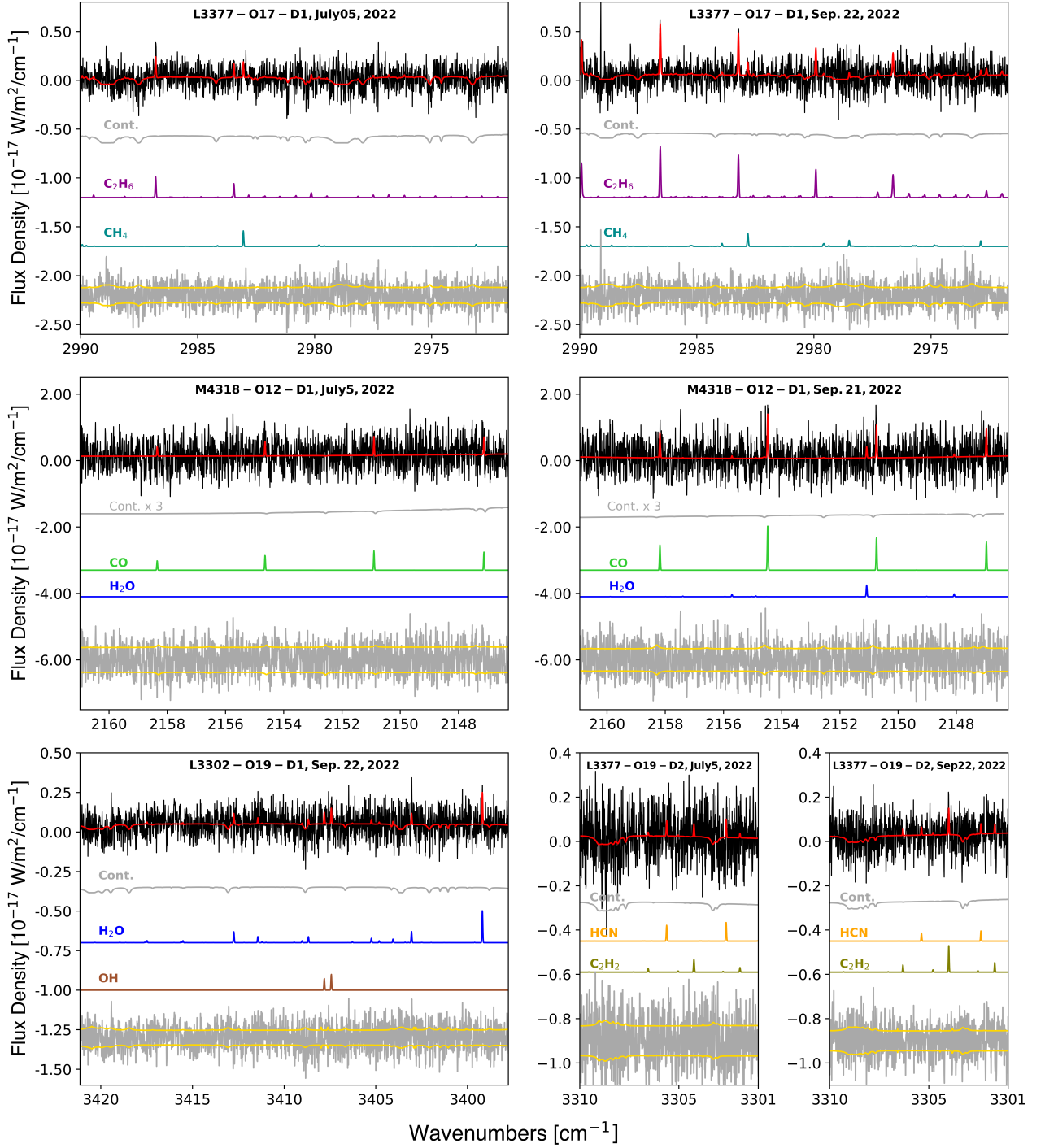
Appendix C: CRIRES⁺ spectra.

Fig. C.1: Spectra of comet C/2017 K2 acquired with CRIRES⁺. In each plot, the top spectrum shows the observed data along with the total model (in red), while the gray spectrum below represents the modeled transmittance. Molecular models used to derive the production rates are displayed in different colors and labeled accordingly. Residuals are shown at the bottom in gray, with yellow lines indicating the $\pm 1\sigma$ uncertainties. Setting, detector number, and observing date are shown on top of each plot.